Analytical Framework for Full Dimensional Massive MIMO with Ray-Based Channels

Chelsea L. Miller, *Student Member, IEEE*, Peter J. Smith, *Fellow, IEEE*, Pawel A. Dmochowski, *Senior Member, IEEE*, Harsh Tataria, *Member, IEEE*, and Michail Matthaiou, *Senior Member, IEEE*

***Abstract*—The performance of baseband beamforming in multi-user multiple-input multiple-output (MU-MIMO) systems has been extensively studied for *simplified statistical* channel models where no angular parameters are taken into account. In contrast, there is little performance analysis with *ray-based* models, which are more physically motivated, feature prominently in standardization and have been experimentally validated. Thus, unlike previous studies, we present a mathematical framework to analyze the performance of zero forcing (ZF) and minimum mean-squared error (MMSE) combining. Using a central result for averaging in the angular domain, we derive tight approximations for the uplink signal-to-noise ratio and signal-to-interference-and-noise ratio (SINR) for ZF and MMSE processing, respectively, and the resulting spectral efficiencies. The remarkably simple expressions offer the following insights into the effects of the propagation environment. We demonstrate an improvement in performance when moving from vertical uniform rectangular array (URA) to horizontal URA to uniform linear array (ULA) antenna configurations. There is also a corresponding increase in the robustness of the performance to propagation scenarios. We demonstrate that under specific conditions increasing the angular spread can *decrease* the SINR for a ULA - an unexpected behavior which we link to the effects of end-fire radiation. Furthermore, our results allow us to investigate the impact of different array configurations and system parameters on the rate of convergence to favorable propagation conditions. Finally, we evaluate the spatial correlation properties intrinsically present in ray-based models, and compare them to the commonly used simple exponential model which yields equal, fixed correlation characteristics for each user.**

***Index Terms*—Ergodic spectral efficiency, favorable propagation, linear processing, MU-MIMO, ray-based channel models.**

I. Introduction

Performance analysis of linear transceiver techniques for conventional and massive multi-user multiple-input multiple-output (MU-MIMO) systems is well advanced for simple statistical channel models [2]–[7]. Early work on independent, identically distributed Rayleigh fading channels has been extended to a wide range of more complex and realistic channel models. For example, results are now emerging on complex, heterogeneous, correlated Ricean channels for both uplink (UL) and downlink (DL) systems employing maximum ratio combining (MRC) [8], zero-forcing (ZF) [9] and minimum mean-squared error (MMSE) combining [10], [11]. In contrast, the literature on performance analysis for ray-based channels is very sparse. In this paper, we use the phrase *ray-based* to denote a wide class of channel models where a user's channel is broken down into a finite set of rays denoting the different multipath components in the channel, as a result of the transmitted waveform interacting with objects in the environment forming different propagation processes. Specific properties of the ray angles can be modeled by statistical distributions obtained from propagation measurements. Broadly speaking, this covers many of the models described as *spatial* or *directional*.

Ray-based models have several advantages over the simplified statistical models: (1) they are more physically motivated; (2) they have a direct link to the antenna layout at both link ends, and to the propagation environment; (3) they are applicable over a wide range of frequency bands. For example, recent ray-based measurements are used to characterize the channel at 2.53 GHz [12] and at 28 GHz and 73 GHz [13]–[15]. For these reasons, ray-based channels form the basis of many standardized models used to evaluate the performance of the upcoming new radio systems [16].

However, the mathematical difficulties attached to such models have systematically obstructed the progress in the performance characterization of linear transceivers. Many papers therefore necessarily focus on numerical simulations [17]–[20]. Some analysis of ray-based models in regard to favorable propagation (FP) and channel hardening has appeared in [21]–[23]. Furthermore, [24] analyzes the achievable rate with maximum ratio transmission (MRT) in the downlink via a simple line-of-sight (LOS) propagation environment. The bulk of the work to date makes restrictive assumptions regarding the ray angles and their angular distributions. For example, it is often assumed that the ray angles [21] are uniform over the whole range (180° in elevation and 360° in azimuth) or the sine of the ray angles [24], [25] is uniform over $[-1, 1]$. More recently, work has appeared on DL MRT and regularized ZF [26] with pilot contamination in ray-based channels but yet again the angles are restricted to be uniformly distributed. In practice, such simple distributions are rarely observed. For instance, recent measurement data [12] has shown that the ray angles in azimuth and elevation domains across multiple clusters are Gaussian and Laplacian distributed, respectively, whereas angles within a cluster are well described by Laplacian distributions. 3GPP channel models [16] also follow a similar form with more complex statistical distributions, which

C. L. Miller and P. A. Dmochowski are with the School of Engineering and Computer Science, Victoria University of Wellington, Wellington, New Zealand (e-mail: {chelsea.miller,pawel.dmochowski}@ecs.vuw.ac.nz).

P. J. Smith is with the School of Mathematics and Statistics, Victoria University of Wellington, Wellington, New Zealand (e-mail: peter.smith@sms.vuw.ac.nz).

H. Tataria is with the Department of Electrical and Information Technology, Lund University, Lund, Sweden (e-mail: harsh.tataria@eit.lth.se).

M. Matthaiou is with the Institute of Electronics, Communications and Information Technology (ECIT), Queen's University Belfast, Belfast, U.K. (e-mail: m.matthaiou@qub.ac.uk).

The work of M. Matthaiou was supported by EPSRC, UK, under grant EP/P000673/1 and by the RAEng/The Leverhulme Trust Senior Research Fellowship LTSRF1718\14\2.

An early version of this work [1] was presented at IEEE ICC 2019, Shanghai, China.

are not treated in the prior state-of-the-art [26]–[30] due to the underlying mathematical complexities. Following this line of reasoning, the models presented in this paper are inherently general and, thus, analysis proves to be extremely challenging.

Although *exact* analysis of linear processing in massive MIMO systems with ray-based models is almost certainly intractable due to the extremely complex nature of the mathematical expressions, we note that moment-based approaches are promising for moderate-to-large system sizes. This observation is based on the fact that expectations of the resulting channel cross products are the building blocks for the analysis of FP, channel hardening, MRT and MRC [31]. This is the area where most analytical work has made progress. Further, we note that moment based approaches were used successfully in [8]–[11] for more involved heterogeneous statistical channel models. The analytical difficulty of handling ray-based models is clearly shown in the following observation. Simpler statistical channel models give rise to matrix channels, $\mathbf{H}$, where the distribution of the elements is trivial and matrix functions such as $\mathbf{H}\mathbf{H}^H$ and $(\mathbf{H}\mathbf{H}^H)^{-1}$, where $(\cdot)^H$ denotes the conjugate transpose operator, often have known distributions based on Wishart matrices. In contrast, for ray-based channels, to the best of our knowledge, even the most basic statistical information, the probability distribution function (PDF) of a channel element, remains *unknown*. Faced with this fundamental problem, we are able to make analytical progress by a careful application of three key insights: 1) the moments of the channel entries are more tractable than the PDF; 2) the large system approximations in [9], [10] suggest that performance can be reduced to such moments; and 3) the moments can be handled in very general environments using a Fourier expansion of the angular PDFs.

Such a methodology was developed in our conference paper [1] for uniform linear arrays (ULAs) using ZF or MRC processing leading to accurate approximations for the ZF signal-to-noise-ratio (SNR). In this work, we extend this approach considerably to handle MMSE processing and full-dimension processing with uniform rectangular arrays (URAs). We also investigate the FP convergence and the underlying spatial correlation structure of ray-based channels. We develop a novel methodology to analyze ZF and MMSE in UL systems for ULAs and URAs and an extremely wide range of angular distributions. This includes all commonly used ray models, such as those containing clusters of rays and angles with wrapped Gaussian and Laplacian distributions. To this end, unlike previous studies in the literature, our work acts as a unified framework for the performance analysis of massive MIMO systems with ray-based propagation. In particular, we make the following contributions:

- We derive accurate approximations to the mean SNR and mean signal-to-interference-and-noise ratio (SINR) of ZF and MMSE combiners, respectively, for large antenna arrays. The results are applicable to different antenna configurations and ray-based channel models with all practical parameter distributions. These remarkably simple, closed-form results deliver many insights into the link between performance and system parameters and ray distributions.
- We evaluate the SNR/SINR and the spectral efficiency (SE), demonstrating an improvement in performance when moving from vertical URA (VURA) to horizontal URA (HURA) to ULA antenna configurations due to the increasing Rayleigh resolution in the diverse azimuth domain. Similarly, we demonstrate an increase in performance robustness to propagation scenarios for such array configurations.
- We demonstrate the seemingly counter-intuitive behavior where under specific conditions increasing the angular spread *decreases* the SINR for a ULA. This behavior is explained through our analytical results and is linked to the effects of end-fire radiation.
- Using the derived expressions, we also investigate the impact of array configurations and system parameters on the rate of convergence to FP.
- Finally, we evaluate the spatial correlation properties intrinsic in ray-based models, comparing them to the commonly used and well understood exponential model.

II. System Model

We examine a single-cell massive MIMO system where a BS with M electronically steerable antenna elements configured as a ULA or URA serves L single-antenna users within a single resource block. We consider UL transmission assuming perfect CSI at the BS.[1]

A. Channel Model

The $M \times 1$ channel vector between the BS and the lth user is modeled by the generic clustered ray-based model [15], [17]

$$\mathbf{h}_l = \sum_{c=1}^{C} \sum_{s=1}^{S} \gamma_{c,s}^{(l)} \mathbf{a}(\theta_{c,s}^{(l)}, \phi_{c,s}^{(l)}), \tag{1}$$

where C is the number of clusters and S is the number of subpaths per cluster. The vector $\mathbf{a}(\theta_{c,s}^{(l)}, \phi_{c,s}^{(l)})$ represents the $M \times 1$ steering vector pertaining to subray s in cluster c as experienced by user l. The azimuth angle of arrival (AoA) of each ray is modeled as $\phi_{c,s}^{(l)} = \phi_c^{(l)} + \Delta_{c,s}^{(l)}$ where $\phi_c^{(l)}$ is the central angle of the rays of cluster c, and $\Delta_{c,s}^{(l)}$ is the deviation of subray s from that central angle. Similarly, the elevation angle is modeled as $\theta_{c,s}^{(l)} = \theta_c^{(l)} + \delta_{c,s}^{(l)}$ where $\theta_c^{(l)}$ is the central angle of the rays of cluster c, and $\delta_{c,s}^{(l)}$ is the deviation of subray s from that central angle.

The ray coefficients, $\gamma_{c,s}^{(l)}$, are modeled as $\gamma_{c,s}^{(l)} = \beta_{c,s}^{(l)1/2} e^{j\Phi_{c,s}^{(l)}}$ where $\beta_{c,s}^{(l)}$ is the ray power and $\Phi_{c,s}^{(l)} \sim \mathcal{U}[0, 2\pi]$ are uniform phases. Hence, the total link gain for user l is $\beta^{(l)} = \sum_{c=1}^{C} \sum_{s=1}^{S} \beta_{c,s}^{(l)}$. The classical path-loss and shadowing model is used for the link gains so that

$$\beta^{(l)} = A X_l \left(\frac{d_l}{d_0} \right)^{-\Gamma}, \tag{2}$$

[1]Although naïve, we note this assumption allows us to quantify an upper bound on system performance in contrast to what may be achieved with imperfect channel knowledge. This scenario also better resembles the use case where there is low terminal mobility, allowing us to dedicate a large fraction of the coherence time for accurate estimation of the downlink channel [32].

where d_l is the distance between user l and the BS, A is the received power at the reference distance d_0 in the absence of shadowing, Γ is the pathloss exponent, and X_l models the effects of shadow fading, taken from a lognormal distribution with zero mean and variance σ_{sf}^2. Once the link gains are generated from (2), the cluster powers, $\beta_c^{(l)}$, are set to decay exponentially from $\beta_1^{(l)}$ to $\beta_C^{(l)}$ in order to create unequal cluster powers. The inter-cluster ratio $\beta_C^{(l)}/\beta_1^{(l)}$ is set at 0.1 for all results. Finally, all subpaths have the same power as in [16], so that $\beta_{c,s}^{(l)} = \beta_c^{(l)}/S$. In this study, we do not consider per-element antenna patterns in the azimuth and elevation domains, since we would like to remove the directional dependence of the elements in order to evaluate the performance upper bound of linear processors. We note that this assumption does not affect the resulting propagation parameters used for further evaluation in the paper, since the majority of the measurements are post processed with high resolution parameter extraction techniques like RiMAX and SAGE in [12], [33], where a double-directional channel response is created from the measured parameters to remove the antenna dependence from the channel measurements, i.e., to make the propagation parameters antenna agnostic.

1) ULA Model: For a ULA, the steering vectors are given by [34]

$$\mathbf{a}(\theta_{c,s}^{(l)}, \phi_{c,s}^{(l)}) = [1, e^{j2\pi d \sin\phi_{c,s}^{(l)}} \dots e^{j2\pi(M-1)d\sin\phi_{c,s}^{(l)}}]^T, \quad (3)$$

where $(\cdot)^T$ denotes the transpose operator, d is the antenna spacing in wavelengths and $\phi_{c,s}^{(l)} = 0$ corresponds to array broadside.

2) Horizontal URA Model: Consider a URA in the $x-y$ azimuth plane as shown in [21], [35] with a total of $M = M_x M_y$ antennas where M_x and M_y are the antenna numbers in the x and y directions, respectively. With this orientation, the Rayleigh resolution is larger in azimuth than elevation. The steering vectors are given by the Kronecker product [21]

$$\mathbf{a}(\theta_{c,s}^{(l)}, \phi_{c,s}^{(l)}) = \mathbf{a}_x(\theta_{c,s}^{(l)}, \phi_{c,s}^{(l)}) \otimes \mathbf{a}_y(\theta_{c,s}^{(l)}, \phi_{c,s}^{(l)}), \quad (4)$$

where $\mathbf{a}_x(\cdot)$ and $\mathbf{a}_y(\cdot)$ are given by

$$[1, e^{j2\pi d_x \sin\theta_{c,s}^{(l)} \cos\phi_{c,s}^{(l)}} \dots e^{j2\pi(M_x-1)d_x \sin\theta_{c,s}^{(l)}\cos\phi_{c,s}^{(l)}}]^T, \quad (5)$$

and

$$[1, e^{j2\pi d_y \sin\theta_{c,s}^{(l)} \sin\phi_{c,s}^{(l)}} \dots e^{j2\pi(M_y-1)d_y \sin\theta_{c,s}^{(l)}\sin\phi_{c,s}^{(l)}}]^T, \quad (6)$$

respectively. The distances d_x and d_y are the antenna spacings in wavelengths in the x and y directions, respectively. The angle $\theta_{c,s}^{(l)} = \pi/2$ corresponds to the azimuth plane and $\phi_{c,s}^{(l)} = 0$ is parallel with the x-axis.

3) Vertical URA Model: Consider a URA in the $x-z$ vertical plane as discussed in [36] with a total of $M = M_x M_z$ antennas where M_x and M_z are the antenna numbers in the x and z directions, respectively. As such, the VURA has greater Rayleigh resolution in the elevation domain than the HURA. The steering vectors are given by the Kronecker product

$$\mathbf{a}(\theta_{c,s}^{(l)}, \phi_{c,s}^{(l)}) = \mathbf{a}_x(\theta_{c,s}^{(l)}, \phi_{c,s}^{(l)}) \otimes \mathbf{a}_z(\theta_{c,s}^{(l)}, \phi_{c,s}^{(l)}), \quad (7)$$

where $\mathbf{a}_x(\cdot)$ and $\mathbf{a}_z(\cdot)$ are given by (5) and

$$[1, e^{j2\pi d_z \cos\theta_{c,s}^{(l)}} \dots e^{j2\pi(M_z-1)d_z\cos\theta_{c,s}^{(l)}}]^T, \quad (8)$$

respectively. The distance d_z is the antenna spacing in the z direction in wavelengths. As for the horizontal array, the angle $\theta_{c,s}^{(l)} = \pi/2$ corresponds to the azimuth plane and $\phi_{c,s}^{(l)} = 0$ is parallel with the x-axis.

B. Instantaneous Per-User SINR and Spectral Efficiency

The received signal at the BS can be written as

$$\mathbf{y} = \rho^{\frac{1}{2}}\mathbf{H}\mathbf{s} + \mathbf{n}, \quad (9)$$

where ρ is the uplink transmit power (assumed equal for all users with no power control), $\mathbf{H} = [\mathbf{h}_1, \mathbf{h}_2, ..., \mathbf{h}_L]$ is the $M \times L$ composite channel matrix and $\mathbf{s} = [s_1, s_2, ..., s_L]^T$ is the vector of user symbols, with $\mathbb{E}[s_i] = 0$ and $\mathbb{E}[|s_i|^2] = 1$. The additive white Gaussian noise at the receiver is $\mathbf{n} \sim \mathcal{CN}(\mathbf{0}, \sigma_n^2\mathbf{I}_{\text{M}})$ where $\sigma_n^2 = 1$ without loss of generality. This received signal is processed using a ZF or MMSE linear receiver at the BS, producing, for user l, the signal

$$y_l = \rho^{\frac{1}{2}}\mathbf{w}_l^H\mathbf{h}_l s_l + \sum_{l' \neq l}^{L} \rho^{\frac{1}{2}}\mathbf{w}_l^H\mathbf{h}_{l'}s_{l'} + \mathbf{w}_l^H\mathbf{n}. \quad (10)$$

The weight vector for user l, $\mathbf{w}_l$, is the lth column of the matrix [37]

$$\mathbf{W}^{\text{ZF}} \triangleq \mathbf{H}(\mathbf{H}^H\mathbf{H})^{-1}, \quad (11)$$

$$\mathbf{W}^{\text{MMSE}} \triangleq \mathbf{H}(\tfrac{1}{\rho}\mathbf{I} + \mathbf{H}^H\mathbf{H})^{-1}, \quad (12)$$

for ZF or MMSE, respectively. The resulting SINR[2] is [37]

$$\text{SINR}_l = \frac{\rho|\mathbf{w}_l^H\mathbf{h}_l|^2}{\rho\sum_{l' \neq l}^{L}|\mathbf{w}_l^H\mathbf{h}_{l'}|^2 + \|\mathbf{w}_l\|^2}, \quad (13)$$

leading to the SE: $\text{SE}_l = \log_2(1 + \text{SINR}_l)$.

III. Average SINR and Spectral Efficiency

We examine the ergodic cell-wide SINR and SE of an arbitrary user, l, by first analyzing the expectation over the ray angles, $\theta_{c,s}^{(l)}$, $\phi_{c,s}^{(l)}$ and phases, $\Phi_{c,s}^{(l)}$. Hence, we average throughout the paper over all the variables in the channel except for the ray powers, $\beta_{c,s}^{(l)}$. This approach is used for two reasons. First, it leads to expressions where the effects of the ray powers can be seen. Secondly, there is a wide variety of models for the $\beta_{c,s}^{(l)}$ terms so further averaging is best done on a case-by-case basis or by simulation. The expected SE is simplified with the following common approximation [9], [33], [34], which is also validated for ray-based models in [1], giving

$$\mathbb{E}_{\theta,\phi,\Phi}[\text{SE}_l] \approx \log_2(1 + \mathbb{E}_{\theta,\phi,\Phi}[\text{SINR}_l]), \quad (14)$$

where $\mathbb{E}_{\theta,\phi,\Phi}[\cdot]$ refers to the expectation over the ray angles and the phases of the ray coefficients. Hence, we derive expressions for $\mathbb{E}_{\theta,\phi,\Phi}[\text{SINR}_l]$ for ZF and MMSE processing. In the following, we omit the expectation operator subscripts for a more compact notation.

With this definition of expectation, we note that the channel model in (1) satisfies the second order properties: $\mathbb{E}[\mathbf{h}_i^H\mathbf{h}_j] =$

[2]Here, we use the generic definition of SINR. With ZF processing, the interference term is eliminated, resulting in an SNR expression.

0 for $i \neq j$ and $\mathbb{E}[\mathbf{h}_i^H \mathbf{h}_i] = M\beta^{(i)}$. This is denoted as Property 1 and is used in various proofs in Sec. III and the Appendices. This follows from the independence of $\mathbf{h}_i$ and $\mathbf{h}_j$ and the following results for the ray coefficients: $\mathbb{E}[\gamma_{c,s}^{(l)}] = 0$ as $\mathbb{E}[e^{j\Phi_{c,s}^{(l)}}] = 0$ and $|\gamma_{c,s}^{(l)}|^2 = \beta_{c,s}^{(l)}$, referred to as Property 2.

A. ZF Processing

It is well known that the ZF SNR for UE l can be written as [37]

$$\mathrm{SNR}_l^{\mathrm{ZF}} = \frac{\rho}{((\mathbf{H}^H\mathbf{H})^{-1})_{l,l}}. \tag{15}$$

Via the approximation motivated and verified in [9], we write

$$\mathbb{E}[\mathrm{SNR}_l^{\mathrm{ZF}}] \approx \frac{\rho}{\mathbb{E}[((\mathbf{H}^H\mathbf{H})^{-1})_{l,l}]}. \tag{16}$$

Since the matrix inverse in (16) is intractable for ray-based models, we adopt the Neumann series approach used in [9]. We write the matrix inverse in the denominator of (15) as

$$\begin{aligned}(\mathbf{H}^H\mathbf{H})^{-1} &= (\mathbb{E}[\mathbf{H}^H\mathbf{H}] + \mathbf{H}^H\mathbf{H} - \mathbb{E}[\mathbf{H}^H\mathbf{H}])^{-1} \\ &= (\mathbf{X} + \mathbf{X}')^{-1} = (\mathbf{I} + \mathbf{X}^{-1}\mathbf{X}')^{-1}\mathbf{X}^{-1}, \end{aligned} \tag{17}$$

where $\mathbf{X} = \mathbb{E}[\mathbf{H}^H\mathbf{H}]$ and $\mathbf{X}' = \mathbf{H}^H\mathbf{H} - \mathbb{E}[\mathbf{H}^H\mathbf{H}]$. As seen in [9] and [38], (17) can be approximated using the second-order Neumann approximation,

$$\begin{aligned}&\mathbb{E}[(\mathbf{I} + \mathbf{X}^{-1}\mathbf{X}')^{-1}\mathbf{X}^{-1}] \approx \\ &\mathbb{E}[(\mathbf{I} - \mathbf{X}^{-1}\mathbf{X}' + \mathbf{X}^{-1}\mathbf{X}'\mathbf{X}^{-1}\mathbf{X}')\mathbf{X}^{-1}] \\ &= \mathbf{X}^{-1} - \mathbf{0} + \mathbf{X}^{-1}\mathbb{E}[\mathbf{X}'\mathbf{X}^{-1}\mathbf{X}']\mathbf{X}^{-1}, \end{aligned} \tag{18}$$

using $\mathbb{E}[\mathbf{X}'] = \mathbb{E}[\mathbf{H}^H\mathbf{H} - \mathbb{E}[\mathbf{H}^H\mathbf{H}]] = 0$, and the fact that $\mathbf{X}$ is deterministic. Expanding the expectation in (18) and simplifying, we obtain

$$\begin{aligned}\mathbb{E}[(\mathbf{H}^H\mathbf{H})^{-1}]_{l,l} &\approx [\mathbf{X}^{-1}\mathbb{E}[\mathbf{H}^H\mathbf{H}\mathbf{X}^{-1}\mathbf{H}^H\mathbf{H}]\mathbf{X}^{-1}]_{l,l} \\ &= \mathbf{X}_{l,l}^{-1}\mathbb{E}[\mathbf{H}^H\mathbf{H}\mathbf{X}^{-1}\mathbf{H}^H\mathbf{H}]_{l,l}\mathbf{X}_{l,l}^{-1}, \end{aligned} \tag{19}$$

which follows since $\mathbf{X} = \mathbb{E}[\mathbf{H}^H\mathbf{H}]$ is diagonal from Property 1, described earlier.

Proposition 1. *The expected ZF SINR for ray-based channels can be approximated by*

$$\mathbb{E}[\mathrm{SNR}_l^{\mathrm{ZF}}] \approx \rho M\beta^{(l)} \left(\frac{1}{\kappa\left(L - \sum_{c=1}^{C}\sum_{s=1}^{S}\beta_{c,s}^{(l)2}/\beta^{(l)2}\right) + 1} \right) \tag{20}$$

where

$$\kappa \triangleq \frac{1}{M^2}\mathbb{E}_{\theta,\phi}\left[|\mathbf{a}^H(\theta_{c,s}^{(l)}, \phi_{c,s}^{(l)})\mathbf{a}(\theta_{\hat{c},\hat{s}}^{(l)}, \phi_{\hat{c},\hat{s}}^{(l)})|^2\right], \tag{21}$$

with $c, \hat{c} \in \{1 \dots C\}, s, \hat{s} \in \{1 \dots S\}, c \neq \hat{c}$, is the interaction power between two independent normalized rays.

Proof: The proof is given in Appendix A. ■

Note that we evaluate κ for different antenna configurations in Sec. IV. Since the maximum cross product of any two steering vectors is M, we see that $0 \leq \kappa \leq 1$. Furthermore, if the independent rays in (21) correspond to two different users then κ is seen to be a measure of the normalized interference between the rays. This interpretation is further explored in Sec. VII. Note that κ was also found to be an important performance metric in [39].

B. MMSE Processing

It is well known that the MMSE SINR can be written as [10]

$$\mathrm{SINR}_l^{\mathrm{MMSE}} = \mathbf{h}_l^H(\tfrac{1}{\rho}\mathbf{I} + \mathbf{H}_l^H\mathbf{H}_l)^{-1}\mathbf{h}_l, \tag{22}$$

where $\mathbf{H}_l = [\mathbf{h}_1, \dots, \mathbf{h}_{l-1}, \mathbf{h}_{l+1}, \dots, \mathbf{h}_L]$. Following the approximation methodology motivated and verified in [10], we rewrite (22) in the following. First, using the matrix inversion lemma, we have

$$\mathrm{SINR}_l^{\mathrm{MMSE}} = \mathbf{h}_l^H\left(\rho\mathbf{I} - \rho^2\mathbf{H}_l(\mathbf{I} + \rho\mathbf{H}_l^H\mathbf{H}_l)^{-1}\mathbf{H}_l^H\right)\mathbf{h}_l. \tag{23}$$

Next we approximate $\mathbf{H}_l^H\mathbf{H}_l/M$ by its large system limit, $\mathbf{Q}_l = \lim_{M\to\infty}\mathbf{H}_l^H\mathbf{H}_l/M$, so that

$$\mathrm{SINR}_l^{\mathrm{MMSE}} \approx \mathbf{h}_l^H\left(\rho\mathbf{I} - \rho^2\mathbf{H}_l(\mathbf{I} + \rho M\mathbf{Q}_l)^{-1}\mathbf{H}_l^H\right)\mathbf{h}_l. \tag{24}$$

The second approximation we use from [10] is to replace the matrix $\mathbf{H}_l(\mathbf{I} + \rho M\mathbf{Q}_l)^{-1}\mathbf{H}_l^H$ by its expected value, defined as $\mathbf{T}_l \triangleq \mathbb{E}[\mathbf{H}_l(\mathbf{I} + \rho M\mathbf{Q}_l)^{-1}\mathbf{H}_l^H]$. Even though the two aforementioned approximations utilize results from large-dimensional random matrix theory, we note that they remain tight even for moderate system dimensions. This is since the expectation in the second approximation tends to stabilize with a moderate value of M. We were inspired to use these approximations from [10] since the authors there considered the use of heterogeneous channels but had not yet considered the ray-based channels with instantaneous angular parameters. This gives the approximation to the mean SINR

$$\mathbb{E}[\mathrm{SINR}_l^{\mathrm{MMSE}}] \approx \mathbb{E}[\mathbf{h}_l^H\left(\rho\mathbf{I} - \rho^2\mathbf{T}_l\right)\mathbf{h}_l]. \tag{25}$$

Proposition 2. *The expected MMSE SINR for ray-based channels can be approximated by*

$$\mathbb{E}[\mathrm{SINR}_l^{\mathrm{MMSE}}] \approx \rho M\beta^{(l)}\left(1 - \kappa\sum_{k=1,k\neq l}^{L}\frac{\rho M\beta^{(k)}}{1 + \rho M\beta^{(k)}}\right). \tag{26}$$

Proof: The proof is given in Appendix B. ■

In terms of accuracy, we note that replacing $\mathbf{H}_l^H\mathbf{H}_l/M$ with its large system limit, $\mathbf{Q}_l$, will be most effective if L and κ are *not* large. We know that κ primarily controls the interference power, so smaller κ will reduce the off-diagonals in $\mathbf{H}_l^H\mathbf{H}_l/M$ and help convergence to the diagonal $\mathbf{Q}_l$. Also, smaller L reduces the number of off-diagonal terms giving a smaller aggregate deviation from $\mathbf{Q}_l$. Convergence depends on large M which further justifies the desirability of small κ for increasing approximation accuracy. This argument also applies to the other approximation steps in Proposition 1 and is numerically evaluated in Sec. VII.

We also note that in the high SNR regime, we have $\rho M\beta^{(k)}/(1 + \rho M\beta^{(k)}) \approx 1$ and with this approximation we have the simplified version of (26) given by

$$\mathbb{E}[\mathrm{SINR}_l^{\mathrm{MMSE}}] \approx \rho M\beta^{(l)}\left(1 - (L-1)\kappa\right) \triangleq \mu_{\mathrm{MMSE}}. \tag{27}$$

Some straightforward algebra shows that

$$\begin{aligned}\log_2\left(1 + \mathbb{E}[\mathrm{SINR}_l^{\mathrm{MMSE}}]\right) &= \log_2\left(1 + \mu_{\mathrm{MMSE}}\right) \\ &\quad + \log_2\left(1 + \frac{\epsilon_2}{\rho M\beta^{(l)}}\right), \end{aligned} \tag{28}$$

where $\epsilon_2 = \left(\kappa \sum_{k=1,k\neq l}^{L} \beta^{(l)}/\beta^{(k)}\right)(1-\kappa(L-1))^{-1}$. Hence, as $\rho \to \infty$ the second term in (28) vanishes and the SE approximation using (27) converges to the equivalent approximation using (26). Conversely, at low SNR both (26) and (27) are $\mathcal{O}(\rho)$ so the error in using (27) is also $\mathcal{O}(\rho)$. Hence, (27) is a convenient indicator of performance across all SNRs. Equation (27) is a remarkably simple result relating performance to the key parameters ρ, M, L, $\beta^{(l)}$ and κ. Note that (27) requires $(L-1)\kappa < 1$ which supports the above discussion where accurate approximations require L and κ to be small. Also, in the high SNR region, ZF and MMSE become very similar so that (27) can also be used as an approximation to $\mathbb{E}[\mathrm{SNR}_l^{\mathrm{ZF}}]$.

C. Implications of the SINR Results

Equations (20), (26) and (27) are powerful tools for interpreting the behavior of ray-based massive MIMO channels. Note that (52) in Appendix B demonstrates that κ has the alternative expression, $\kappa = \|\mathbf{A}\|_{\mathrm{F}}^2/M^2$, where $\mathbf{A} = \left(\beta^{(i)}\right)^{-1}\mathbb{E}[\mathbf{h}_i\mathbf{h}_i^H]$ and $\|\cdot\|_{\mathrm{F}}^2$ is the Frobenius norm. Hence, κ can be interpreted both as the interference power between two rays and also as the normalized squared Frobenius norm of the channel correlation matrix. This allows the SINR results in Proposition 1 and Proposition 2 to be interpreted in a familiar way as functions of system size, SNR, channel power and channel correlation. We immediately see the adverse effect of correlation on SNR/SINR as both $\mathrm{SNR}_l^{\mathrm{ZF}}$ and $\mathrm{SINR}_l^{\mathrm{MMSE}}$ are decreasing functions of κ. We note that channel hardening has been observed in a recent measurement campaign [40] where it was found that measured indoor channels do experience channel hardening but more slowly than i.i.d. Rayleigh channels. This experimental work supports the approximations used in (17) and (24) which partly depend on channel hardening. The results in Sec. VII also align with [40] as it is shown that both κ and SINR performance improve for wider angular spreads, where i.i.d. Rayleigh can be seen as an extreme case.

ZF Processing: From (20), we observe the following key properties. As $\rho \to \infty$, the SNR grows linearly with ρ due to the interference cancellation of perfect ZF. As $M \to \infty$, the SNR grows asymptotically linearly with M. Similarly, the SNR grows asymptotically linearly with $\beta^{(l)}$. We observe that the *spread* of ray powers plays only a minor role. In the denominator of (20), the term $\sum_{c=1}^{C}\sum_{s=1}^{S}\beta_{c,s}^{(l)2}$ is affected by the spread. However, this term is small relative to $L\beta^{(l)2}$ and $M\beta^{(l)}$. Hence, the effect of the spread of the ray powers is usually dominated by the terms involving the total power, $\beta^{(l)}$, especially when L and/or M are large (see [1]).

The distribution of the ray angles affects the mean SINR only through the term κ. Hence, we discuss the impact of κ in more detail. The link between κ and the actual angular PDF is not obvious as κ has a relatively complex formulation. Nevertheless, the trends can be inferred from the interpretation of κ in (21) as the interaction power between two distinct and independent rays. For small numbers of antennas and URAs, traditional thinking applies. Angular PDFs with larger variance (wider angular spread) spread the rays, reducing the chance of two rays being similar and hence reducing interference. Therefore, increased angular spread is beneficial for small numbers of antennas. For large numbers of antennas in a ULA the situation is different and more complex. Substituting the ULA steering vector from (3) into (21), gives

$$\kappa = \frac{1}{M^2}\mathbb{E}\left[\left|\sum_{m=0}^{M-1} e^{j2\pi dm\left(\sin\phi_{\hat{c},\hat{s}}^{(l)} - \sin\phi_{c,s}^{(l)}\right)}\right|^2\right]. \tag{29}$$

The maximum of the variable in (29) occurs at $\sin\phi_{c,s}^{(l)} = \sin\phi_{\hat{c},\hat{s}}^{(l)}$ so it is important to identify scenarios where very close agreement between the sines of the ray angles occurs. Since the sine function changes most rapidly around 0 (broadside), close agreement near broadside is less likely. However, the sine function changes least rapidly near $\pm\pi/2$ (end-fire) so here close agreement is more likely. This observation is more important for large M as $\kappa \leq 1$. Hence, for large numbers of antennas in a ULA, increased angular spread puts more ray powers near to end-fire which inflates κ. Thus, a crossover occurs where larger angular spread increases SINR for smaller numbers of antennas and decreases SINR for larger numbers. This is partly demonstrated in Sec. VII (Fig.1) where κ initially drops and then increases as σ_{s} is increased for a fixed number of antennas, $M = 144$. In contrast to the URAs where wider angular spread is always beneficial we see that increased spread can hurt ULA performance and can even cause it to become worse than that with narrower spreads. In Sec. VII (Fig. 5) we show that κ can decrease with increasing angular spread for small M, yet increase for large M.

Note that the sectoral antennas envisaged for massive MIMO have finite angular range radiation patterns in both the azimuth and elevation domains [16]. Hence, radiation near end fire is substantially attenuated and this will reduce the visibility of these unexpected trends.

MMSE Processing: The trends shown by (26) are the same as ZF for M, ρ and the ray powers: asymptotic linear growth in M, ρ and $\beta^{(l)}$. For MMSE also, large values of κ reduce the SINR.

IV. Averaging in the Angular Domain

The SINR expressions in (20) and (26) both require κ which can be computed as follows for the three antenna layouts discussed in Sec. II. Substituting the steering vectors for the ULA into (21) and defining θ, ϕ as a generic pair of ray angles and $\hat{\phi}$ as a second azimuth angle independent of ϕ gives

$$\begin{aligned}\kappa &= \frac{1}{M^2}\mathbb{E}\left[\sum_{m=0}^{M-1}\sum_{n=0}^{M-1} e^{j2\pi d(m-n)(\sin\hat{\phi}-\sin\phi)}\right] \\ &= \frac{1}{M^2}\sum_{m=0}^{M-1}\sum_{n=0}^{M-1}\mathbb{E}[e^{-j2\pi d(m-n)\sin\phi)}]\mathbb{E}[e^{j2\pi d(m-n)\sin\hat{\phi})}] \\ &= \frac{1}{M^2}\sum_{m=0}^{M-1}\sum_{n=0}^{M-1}\left|\mathbb{E}\left[e^{j2\pi d(m-n)\sin\phi)}\right]\right|^2. \end{aligned} \tag{30}$$

for a ULA. A similar process gives κ as

$$\frac{1}{M^2}\sum_{m_x,n_x}^{M_x-1}\sum_{m_y,n_y}^{M_y-1}\left|\mathbb{E}\left[e^{j2\pi\sin\theta[(m_x-n_x)d_x\cos\phi+(m_y-n_y)d_y\sin\phi]}\right]\right|^2, \tag{31}$$

for an HURA and

$$\frac{1}{M^2}\sum_{m_x,n_x}^{M_x-1}\sum_{m_y,n_y}^{M_y-1}\left|\mathbb{E}\left[e^{j2\pi[(m_x-n_x)d_x\sin\theta\cos\phi+(m_z-n_z)d_z\cos\theta]}\right]\right|^2, \tag{32}$$

for a VURA. In (31) and (32), the summation notation $\sum_{i,j}^{I-1}$ refers to the double sum $\sum_{i=0}^{I-1}\sum_{j=0}^{I-1}$.

Hence, κ involves expectations of various exponentials of trigonometric functions. We begin the analysis by considering the ULA case, where the expectation required in (30) is of the form $\mathbb{E}[e^{jz\sin\phi}]$ where $z = 2\pi d(m-n)$ for $m,n \in \mathbb{Z}$ and ϕ is the azimuth AoA of an arbitrary user's ray written as $\phi = \phi_c + \Delta$, where ϕ_c is the central cluster angle and Δ is the subray offset.

Lemma 1. *We have $\mathbb{E}[e^{jz\sin\phi}] = \sum_{n=-\infty}^{\infty}\psi(n)J_n(z)$, where $\psi(n)$ is the characteristic function (CF) of ϕ, $\psi(n) = \mathbb{E}[e^{jn\phi}]$, and $J_n(\cdot)$ is the nth order Bessel function of the first kind.*

Proof: The proof is given in Appendix C. ■

As the rays are modeled in clusters, we have

$$\begin{aligned}\psi(n) &= \mathbb{E}[e^{jn\phi}] = \mathbb{E}[e^{jn(\phi_c+\Delta)}]\\ &= \mathbb{E}[e^{jn\phi_c}]\mathbb{E}[e^{jn\Delta}] = \psi_c(n)\psi_s(n),\end{aligned}$$

where $\psi_c(n)$ and $\psi_s(n)$ are the CFs of the central cluster angles and subray offsets. From Lemma 1, we have the *exact* solution

$$\mathbb{E}[e^{jz\sin\phi}] = \sum_{n=-\infty}^{\infty}\psi_c(n)\psi_s(n)J_n(z). \tag{33}$$

Note that (33) is completely general and applies to any clustered ray-based model where $\phi_{c,s} = \phi_c + \Delta_{c,s}$. Furthermore, in most cases the CFs decay very rapidly so that (33) can be approximated by a small number of terms. For example, a common model is to have a wrapped normal distribution for ϕ_c, $\phi_c \sim \mathcal{N}(\mu_c, \sigma_c^2)$, and a Laplacian for $\Delta_{c,s}$, $\Delta_{c,s} \sim \mathcal{L}(\frac{1}{\sigma_s})$, so that the PDF of $\Delta_{c,s}$ is $f_\Delta(x) = (2\sigma_s)^{-1}\exp(-|x|/\sigma_s)$. This choice gives the CFs $\psi_c(n) = \exp(jn\mu_c - n^2\sigma_c^2/2)$ and $\psi_s(n) = (1+n^2\sigma_s^2)^{-1}$. This specific solution gives

$$\mathbb{E}[e^{jz\sin\phi}] = \sum_{n=-\infty}^{\infty}\frac{e^{jn\mu_c-\frac{n^2\sigma_c^2}{2}}}{1+n^2\sigma_s^2}J_n(z). \tag{34}$$

Note that the coefficients of $J_n(z)$ behave like $n^{-2}\exp(-n^2\sigma_c^2/2)$ and therefore decay very quickly. Hence, a reasonable approximation may be obtained through $2N+1$ terms of the summation, giving

$$\mathbb{E}[e^{jz\sin\phi}] \approx \sum_{n=-N}^{N}\frac{e^{jn\mu_c-\frac{n^2\sigma_c^2}{2}}}{1+n^2\sigma_s^2}J_n(z). \tag{35}$$

Note that any desired accuracy in (35) can be obtained by choosing N as in Appendix F. Next, we consider the HURA where the expectation required in (31) is of the form

$$H_h(z_1,z_2) \triangleq \mathbb{E}\left[e^{jz_1\sin\theta\sin\phi+jz_2\sin\theta\cos\phi}\right]. \tag{36}$$

Lemma 2. *$H_h(z_1,z_2)$ as defined in (36) is given by*

$$H_h(z_1,z_2) = \sum_{m=-\infty}^{\infty}\sum_{n=-\infty}^{\infty}(-1)^{p(n)}\psi(n)\chi(2m)e^{jnA}I(m,n), \tag{37}$$

where $p(n) = 0$ for $n \geq 0$, $p(n) = n$ for $n < 0$, $A = tan^{-1}(z_2/z_1)$ and $I(m,n)$ is given by

$$I(m,n) = J_{\frac{|n|}{2}-m}\left(\sqrt{\frac{z_1^2+z_2^2}{4}}\right)J_{\frac{|n|}{2}+m}\left(\sqrt{\frac{z_1^2+z_2^2}{4}}\right). \tag{38}$$

The CF, $\psi(\cdot)$ is given in Lemma 1 and $\chi(\cdot)$ is the CF of θ given by $\chi(n) = \mathbb{E}[e^{jn\theta}] = \mathbb{E}[e^{jn(\theta_c+\delta)}] = \mathbb{E}[e^{jn\theta_c}]\mathbb{E}[e^{jn\delta}] = \chi_c(n)\chi_s(n)$ where $\chi_c(n)$ and $\chi_s(n)$ are the CFs of the elevation central cluster angle and the elevation offsets respectively.

Proof: The proof is given in Appendix D. ■

Finally, we consider the VURA where the expectation required in (32) is of the form

$$H_v(z_1,z_2) \triangleq \mathbb{E}\left[e^{jz_1\cos\theta+jz_2\sin\theta\cos\phi}\right]. \tag{39}$$

Lemma 3. *$H_v(z_1,z_2)$ as defined in (39) is given by*

$$\sum_{n=-\infty}^{\infty}e^{jn\pi/2}\psi(n)\int_0^{\pi}e^{jz_1cos\theta}J_n(z_2sin\theta)f_w(\theta)d\theta, \tag{40}$$

where $f_w(\theta)$ is the wrapped PDF of θ on $[0,\pi]$.

Proof: The proof is given in Appendix E. ■

At present no further convenient analysis for $H_v(z_1,z_2)$ appears tractable and we leave the representation in Lemma 3 as a single finite range numeric integral. Substituting the results of Lemmas 1, 2 and 3 in (30), (31) and (32), respectively, gives κ which completes the derivation of (20) and (26). As for the ULA, we note that summation over n can be truncated with very few terms as the $\psi(n)$ coefficients decay very rapidly. In Appendix F we prove the convergence of the series in Lemmas 1, 2, and 3 and also derive bounds on the truncation error of these series. This allows us to select the number of terms in the truncated series to guarantee any desired accuracy.

V. Favorable Propagation

Originally introduced in [25], FP concerns the normalized interference between two users. One of the major advantages of massive MIMO is that this interference often vanishes as $M \to \infty$. Such a behavior is described as FP. Together with channel hardening, a consequence of FP is that $\frac{1}{M}\mathbf{H}^H\mathbf{H}$ converges to a diagonal matrix. Although well-studied for classical statistical channel models [41], less is known about FP for ray-based models. In [21], it was shown that FP holds for uniform angular distributions. More generally, for a ULA, it has been shown that FP does occur with ray-based channels [31] for an extremely wide range of angular distributions.[3] This implies that the normalized interference between two users $\mathbf{h}_i^H\mathbf{h}_j/M$ vanishes as $M \to \infty$. However, [31] also demonstrates that $\mathbb{E}[|\mathbf{h}_i^H\mathbf{h}_j|^2/M] \to \infty$ as $M \to \infty$. Hence, the rate at which FP occurs is likely to be slow. Using the

[3]This conclusion is extended to URAs in a forthcoming paper.

results in Sec. IV, we are able to assess this rate by calculating $\mathrm{Var}(\mathbf{h}_i^H\mathbf{h}_j/M)$ (as suggested in [25]). Since $\mathbb{E}[\mathbf{h}_i] = 0$, we have

$$\mathrm{Var}\left(\frac{\mathbf{h}_i^H\mathbf{h}_j}{M}\right) = \frac{1}{M^2}\mathbb{E}[\mathbf{h}_i^H\mathbf{h}_j\mathbf{h}_j^H\mathbf{h}_i]. \tag{41}$$

From Appendix B we have $\mathbb{E}[\mathbf{h}_j\mathbf{h}_j^H] = \beta^{(j)}\mathbf{A}$ and $\mathbb{E}[\mathbf{h}_i^H\mathbf{A}\mathbf{h}_i] = \beta^{(i)}M^2\kappa$, where $\mathbf{A}$ is defined in Appendix B. Hence, we have

$$\mathrm{Var}\left(\frac{\mathbf{h}_i^H\mathbf{h}_j}{M}\right) = \beta^{(i)}\beta^{(j)}\kappa, \tag{42}$$

and we observe again, the importance of the κ parameter in determining not only ZF and MMSE performance, but also the rate at which FP occurs. In summary, while the interference term $\mathbf{h}_i^H\mathbf{h}_j/M$ vanishes as $M \to \infty$, the rate at which it vanishes is controlled by κ as in (42). In Sec. VII, this rate is explored numerically using (42). Note that (42) reinforces the interpretation of κ as an interference measure as it is proportional to the normalized interference between channels $\mathbf{h}_i$ and $\mathbf{h}_j$.

VI. Correlation Structure

In [42] it was shown that the summation over the CS uniform phases in the ray coefficients leads to channel elements which are very closely approximated by Gaussian variables. Hence, ray-based channels can often be interpreted as similar to correlated Gaussian channels where the Gaussianity arises via the summation over the random phases and the correlation structure is user-specific and driven by the ray powers and the angles of the rays.[4] From (1) and the properties of the $\gamma_{c,s}^{(l)}$ coefficients we average over the ray phases only to obtain the local correlation matrix, $\mathbf{R}_l$, for user l as

$$\begin{aligned}\mathbb{E}_\Phi[\mathbf{h}_l\mathbf{h}_l^H] &= \mathbb{E}_\Phi\left[\sum_{c,s}^{C,S}\sum_{\hat{c},\hat{s}}^{C,S}\gamma_{c,s}^{(l)}\gamma_{\hat{c},\hat{s}}^{(l)*}\mathbf{a}(\theta_{c,s}^{(l)},\phi_{c,s}^{(l)})\mathbf{a}^H(\theta_{\hat{c},\hat{s}}^{(l)},\phi_{\hat{c},\hat{s}}^{(l)})\right]\\ &= \sum_{c=1}^{C}\sum_{s=1}^{S}\beta_{c,s}^{(l)}\mathbf{a}(\theta_{c,s}^{(l)},\phi_{c,s}^{(l)})\mathbf{a}^H(\theta_{c,s}^{(l)},\phi_{c,s}^{(l)})\\ &\triangleq \beta^{(l)}\mathbf{R}_l.\end{aligned} \tag{43}$$

In Sec. VII, the amount of correlation for ray-based channels is explored by evaluating the square of the Frobenius norm, $||\mathbf{R}_l||_F^2$, of the correlation matrix. This is compared to the simple baseline case of an exponential correlation matrix, $\mathbf{R}^{\text{exp}}$, where the (i,j)-th element is $\alpha^{|i-j|}$ and $0 < \alpha < 1$ controls the correlation level.

VII. Numerical Results

Unless otherwise stated, the numerical results were generated using parameter values in Table I. The users were randomly located in a cell of radius r, outside an exclusion radius r_0. The parameter ρ was chosen such that the median SNR, defined as $\mathrm{SNR}_l = \frac{\rho\beta_l}{\sigma_n^2}$, was -5 dB. The cell wide performance statistics were computed for 10^3 user locations ('drops') and the associated link gains, $\beta^{(l)}$ in (2). For each drop, the average over the ray angles and ray coefficient phases was evaluated using the appropriate analytical expressions in Secs. III and IV. These results were validated via simulation, where numerical averaging was performed over 10^3 angles drawn from the distributions described in Sec. IV. In particular, following [12] for the types of distributions used, we assume a wrapped Gaussian for the central azimuth angle, $\phi_c^{(l)} \sim \mathcal{N}(\mu_\mathrm{c}, \sigma_\mathrm{c}^2)$, a Laplacian for the azimuth offsets $\Delta_{c,s}^{(l)} \sim \mathcal{L}(1/\sigma_\mathrm{s})$, a Laplacian for the central elevation angle $\theta_c^{(l)} \sim \mathcal{L}(1/\hat{\sigma}_\mathrm{c})$ centred on 90° and a Laplacian for the elevation offsets, $\delta_{c,s}^{(l)} \sim \mathcal{L}(1/\hat{\sigma}_\mathrm{s})$. Parameters for these distributions are given in Table I. Note that the analysis can be used for any angular distributions with known CFs. The performance metrics in Sec. VII, labeled $\mathbb{E}[\mathrm{SNR}_l^{\mathrm{ZF}}]$, $\mathbb{E}[\mathrm{SINR}_l^{\mathrm{MMSE}}]$ and $\mathbb{E}[\mathrm{SE}_l^{\mathrm{MMSE}}]$, are to be understood as the averaged values, where the averaging is over the ray angles and phases for a single drop of $\beta_{c,s}^{(l)}$ values. We consider the following two scenarios. Scenario 1, representing a relatively sparse channel with a narrow angular spread, is based on the recent measurement data in [12]. From [12] we use the values of Γ, σ_sf, C, S, σ_c, σ_s and the lower 10% values of the lognormally distributed values of $\hat{\sigma}_\mathrm{c}$ and $\hat{\sigma}_\mathrm{s}$. Scenario 2, which represents a richer scattering environment with a wider angular spread, is based on both [12] and [16]. This scenario uses the same values of Γ and σ_sf. The wider angular spreads are based on the upper 90% values of the lognormally distributed values of $\hat{\sigma}_\mathrm{c}$ and $\hat{\sigma}_\mathrm{s}$ in [12]. Values of C, S, σ_c, σ_s are taken from [16]. Other measurement campaigns at similar frequencies in non line-of-sight urban macrocell environments tend to give values which are bracketed by the two scenarios [17], [43].

Figs. 1 to 4 investigate the effects of the angular parameters, the array types and the number of rays on performance. Hence, each figure contains results for Scenarios 1 and 2 and the three array types (ULA, HURA and VURA) with $M = 144$ and assuming a 12×12 layout for the URAs. All URA results are calculated for $M_x = M_y = M_z = \sqrt{M}$.

Fig. 1 plots κ vs σ_s using (30), (31) and the results of Lemmas 1 and 2 for the ULA and HURA respectively, and the

TABLE I
Parameters for Numerical Results

Parameter	Values
cell radius, r	100 m
exclusion radius, r_0	10 m
median SNR value	-5 dB
pathloss exponent, Γ	3.8
shadow fading standard deviation, σ_sf	5.5 dB
link gain reference distance, d_0	1 m
antenna spacing, d, d_x and d_y	0.5
number of users, L	4
number of clusters, C, (Scen. 1, Scen. 2)	3, 20
number of subrays, S, (Scen. 1, Scen. 2)	16, 20
Azimuth values	
cluster angle mean, μ_c	0°
cluster angle variance, σ_c^2, (Scen. 1, Scen. 2)	$(14.4°)^2$, $(31.64°)^2$
subray angle variance, σ_s^2, (Scen. 1, Scen. 2)	$(6.24°)^2$, $(24.25°)^2$
Elevation values	
cluster angle mean, $\hat{\mu}_\mathrm{c}$	90°
cluster angle variance, $\hat{\sigma}_\mathrm{c}^2$, (Scen. 1, Scen. 2)	$(1.9°)^2$, $(6.12°)^2$
subray angle variance, $\hat{\sigma}_\mathrm{s}^2$, (Scen. 1, Scen. 2)	$(1.37°)^2$, $(1.84°)^2$

[4]This interpretation begins to break down for extreme scenarios with limited number of rays and limited angular spread.

simulated results of (21) for VURA. This can be interpreted in terms of κ as a measure of interference or as a correlation metric as discussed in Sec. III-C. Several of the key properties of the angular parameters are shown here. First, the VURA suffers from the highest interference or correlation as κ is larger. This is followed by the HURA and then the ULA. This is caused by the fact that the azimuth domain has considerably more diversity than the elevation domain for these parameters and the ULA is wider in azimuth than the HURA, which in turn is wider than the VURA. The gap between the scenarios is greater for the URAs than the ULA as the URAs are affected by the increased spread in both azimuth and elevation. Also, the URAs suffer higher interference so any increased spread has a greater impact. In general, increased diversity reduces κ and this is true for both URAs in Fig. 1 where Scenario 1 is worse than Scenario 2 and the curves decay with σ_{s}. For the ULA, we have the unusual behavior caused by the end-fire problem discussed in Sec. III-C. Note that the value of σ_{s} required for the cross-over in the ULA curves is 27° which is higher than that in Scenarios 1 and 2. Hence, the unusual ULA behavior shown here is caused by large angular spreads and is not obvious in the following results which focus on Scenarios 1 and 2.

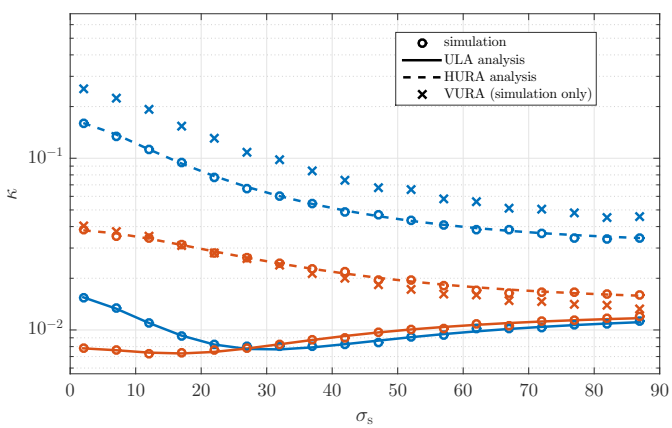

Fig. 1. κ vs σ_{s} for three array types and Scenarios 1 (in blue) and 2 (in red).

Fig. 2 shows the CDFs of $\mathbb{E}[\mathrm{SNR}_l^{\mathrm{ZF}}]$ with the analytical results obtained via Proposition 1 and Lemmas 1 and 2. As with all presented CDFs, the range of values arises from the multiple drops so that each point on the CDF corresponds to a different set of ray powers. The results indicate that ZF SNR performance follows the same broad trends exhibited in Fig. 1: the SNR increases from Scenario 1 to 2 and from the VURA to the HURA to the ULA due to reduced interference caused by higher ray numbers, wider angular spread and a wider azimuth footprint. Although Fig. 1 suggests the ULA can show worst performance for higher spreads, this is not observed here as Scenarios 1 and 2 are not sufficiently rich for this phenomenon to occur. The results also show the very high accuracy of (20) for a wide range of parameter values. The improvement in performance from Scenario 1 to Scenario 2 is greatest for the VURA and least for the ULA, as discussed in Fig. 1, since the impact of the angular parameters is captured by the κ parameter.

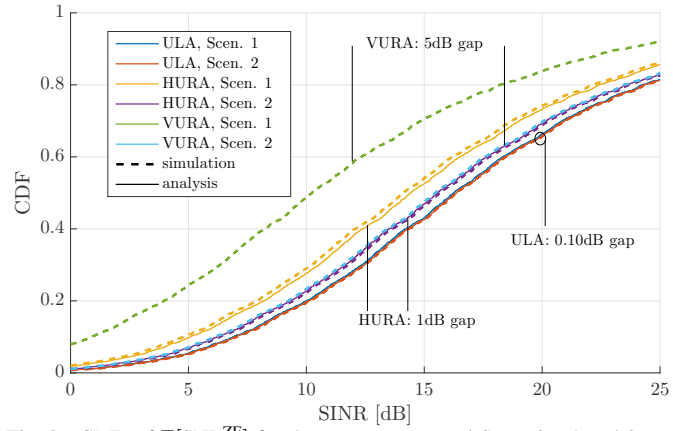

Fig. 2. CDFs of $\mathbb{E}[\mathrm{SNR}_l^{\mathrm{ZF}}]$ for three array types and Scenarios 1 and 2.

Fig. 3 shows the CDFs of $\mathbb{E}[\mathrm{SINR}_l^{\mathrm{MMSE}}]$ with the analytical results obtained via Proposition 2 and Lemmas 1 and 2. Exactly the same trends are observed for MMSE procesing as for ZF and the analysis remains very accurate. A comparison of Fig. 3 and Fig. 2 shows the expected small improvement of MMSE over ZF. As reported in [37], [44], [45], performance of MMSE combining relative to ZF is superior at low SNRs, and equivalent at high SNRs. At the moderate SNR values between -5 and 5 dB, a negligible difference is observed. The differences at low SNRs are due to noise inflation in ZF processing, leading to poor conditioning of the matrix inverse. This has been validated for the extreme cases of i.i.d. Rayleigh fading, and LOS channels [7], [37], [45]. Since the ray-based channel with finite multipath components falls in between these cases, the performance differences between ZF and MMSE are not pronounced in realistic operating regimes, and the overall trends will remain the same.

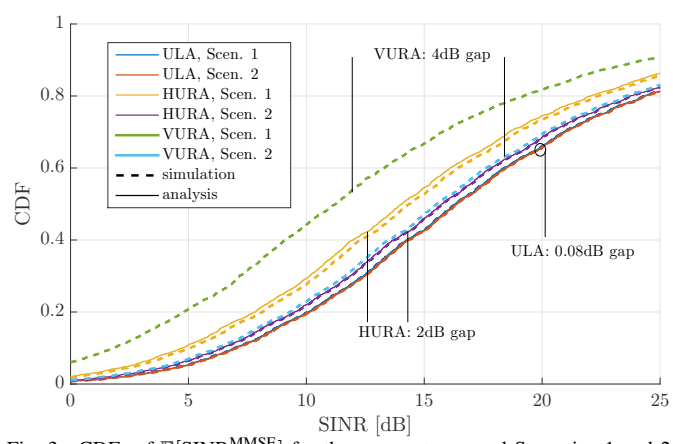

Fig. 3. CDFs of $\mathbb{E}[\mathrm{SINR}_l^{\mathrm{MMSE}}]$ for three array types and Scenarios 1 and 2.

Fig. 4 shows the CDFs of $\mathbb{E}[\mathrm{SE}_l^{\mathrm{MMSE}}]$, with the analytical results obtained via Proposition 2, Lemmas 1 and 2 and the SE approximation in (14). Exactly the same trends are observed as in Fig. 2 and Fig. 4 and the extra approximation in (14) is shown to give accurate results. As discussed at the end of Sec. III-B this accuracy relies on the condition $\kappa \ll 1/(L-1)$. A formal, mathematical characterization of the approximation accuracy for both ZF and MMSE is enormously challenging due to the complexity of the ray-based channels. For example, with ray-based channels there is not even a known PDF for

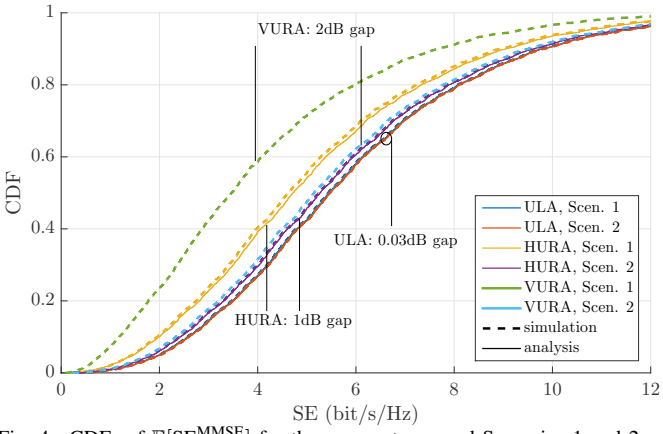

Fig. 4. CDFs of $\mathbb{E}[\mathrm{SE}_l^{\mathrm{MMSE}}]$ for three array types and Scenarios 1 and 2.

TABLE II
MAXIMUM VALUE OF L FOR AN ERROR BELOW 1dB IN (20) AND (26)

ULA						
	$M = 100$			$M = 144$		
Scen.	κ	ZF	MMSE	κ	ZF	MMSE
1	0.01958	27-28	38-39	0.01387	39	54-55
2	0.01055	47-48	77	0.007543	67-68	108-109
HURA						
	$M = 100$			$M = 144$		
Scen.	κ	ZF	MMSE	κ	ZF	MMSE
1	0.1781	4-5	4-5	0.1507	5-6	5-6
2	0.06916	10-11	10-11	0.05433	12-13	12-13

the channel elements. Hence, in the following, we provide a simulation based assessment. Specifically, we investigate the maximum values of L for which expressions (20) and (26) are accurate to within 1dB of the simulated average SINR. These values are found by simulation for Scenarios 1 and 2, $M \in \{100, 144\}$, a ULA/HURA and both ZF and MMSE processing. The values are tabulated in Table II and the associated κ value is also given. We note that accuracy is good for a ULA and for a HURA with wider angle spread. For a HURA with narrow angle spread, accuracy requires a smaller number of users. As predicted in Sec. III-B, accuracy is well reflected by the value of $\kappa(L-1)$. We find that $\kappa(L-1) \leq 0.5$ for all values in Table II. Hence, $\kappa(L-1) \leq 0.5$ can be considered as a rough rule-of-thumb for accuracy of the approximations. Figs. 5-6 show the effect of antenna numbers on performance, FP and the accuracy of the analytical results. Fig. 5 shows how κ changes with M with results generated by the same method used in Fig. 1. The effects of κ vs $0.5/(L-1)$ on both the system performance and the approximation accuracy are clearly observed here. First, as the κ curves move further below the $0.5/(L-1)$ reference (plotted in gray), the corresponding mean SINR seen in Fig. 6 increases, as predicted by (27). At the same time, the approximation accuracy improves when $\kappa < 0.5/(L-1)$. Hence, we expect very tight agreement for ULA antenna configurations, and less so for HURA with small M - again confirmed by Fig. 6.

Also shown in Fig. 5 is the unusual end-fire effect for a ULA discussed in Fig. 1. For very large angle spreads (plotted in green), κ is actually higher than for Scenario 2 as the wide angular spread gives rise to large interference at end-fire. The inset also shows that for large M there is a cross-over and the widest angular spread has a higher value of κ even compared to Scenario 1.

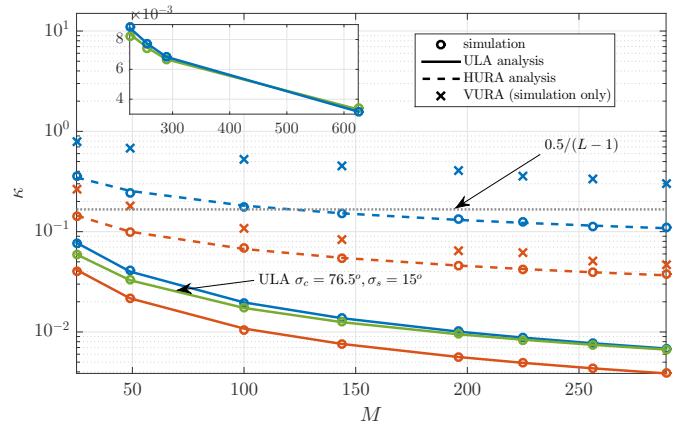

Fig. 5. κ vs M for three array types and Scenarios 1 (in blue) and 2 (in red). A third scenario with extra wide angular spread is shown for a ULA in green and defined in the figure.

Fig. 6 plots the global mean SINR for MMSE processing as a function of M. The y-axis is therefore $\overline{\mathrm{SINR}}_l^{\mathrm{MMSE}} \triangleq \mathbb{E}_\beta[\mathbb{E}[\mathrm{SINR}_l^{\mathrm{MMSE}}]]$ with the SINR being averaged over angles and phases as before and also over the ray powers, as denoted by the $\mathbb{E}_\beta$ operator. As predicted by the analysis, the global

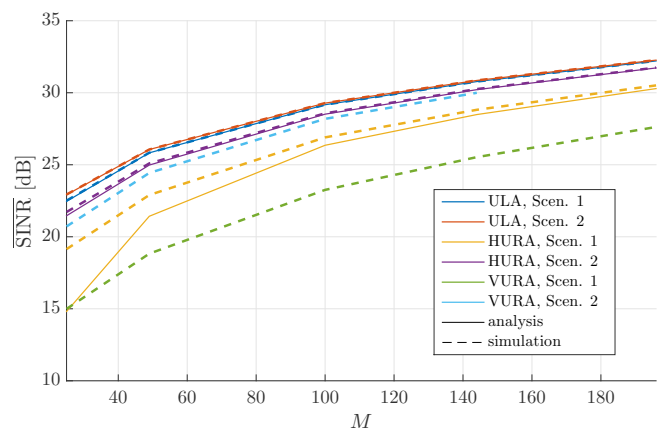

Fig. 6. Global mean SINR for MMSE vs M for three array types and Scenarios 1 and 2.

mean SINR grows asymptotically linearly with M and the relative performance is the same as in Fig. 4 following the established pattern for the impact of the scenarios and the array types. Also shown in Fig. 6 is the loss of analytical accuracy for the least diverse case (HURA with Scenario 1) with smaller array size. As predicted in Sec. III-B, and shown in Fig. 5 the conditions for accuracy begin to break down for smaller arrays and narrow angular spreads. Hence, while the ULA and (HURA, Scenario 2) environments show accurate results over the whole range of M, the (HURA, Scenario 1) environment loses accuracy below $M = 100$.

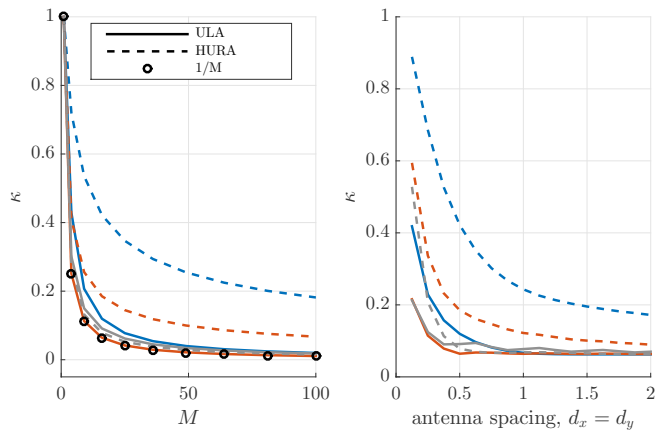

Fig. 7. Left: κ vs M comparison of Scenario 1 (blue), Scenario 2 (red), and uniform angular distribution (grey). Right: κ vs d_x for Scenarios 1 and 2, and uniform angular distribution.

Figure 7 shows κ vs the number of BS antennas and κ vs antenna spacing (for $M = 16$ to reproduce the results in [39]). A comparison is made between the angular distributions used herein and a spherically uniform angular distribution. The latter distribution is used in several previous works including [21], [39]. The uniform angular distribution is appealing as it creates a more mathematically tractable form of the integral in (53) in Appendix C. However, physical measurements such as those in [12] suggest that quite different distributions are required for modeling realistic urban environments. In the left sub-figure we see that antenna topology has little effect on κ vs M for the spherical uniform distribution and all results behave like the rich-scattering result in [39] where κ behaves like $1/M$. With the angular distributions used in the two scenarios, there is a small impact on κ vs M for a ULA and a pronounced effect for an HURA. Hence, topology does have an impact for the typical wrapped Gaussian/Laplacian distributions motivated by measurements. This is re-inforced in the right sub-figure where κ vs antenna spacing is seen to be similar for a ULA and a HURA with uniform angles above $d_x = 0.3$; it should be noted that most practical deployments use an antenna spacing of 0.5 wavelengths or greater. In contrast, the HURA has large differences between the two scenarios and the two topologies are seen to behave differently.

Finally, in Fig. 8 we examine the effects of the angular spread, array type and the number of rays on the spatial correlation at the BS. Specifically, we consider the local correlation matrix, $\mathbf{R}_l$, of user l defined in (43). Fig. 8 plots the CDF of $\frac{1}{M}\|\mathbf{R}_l\|_F^2$ for the two scenarios and three array types with $M = 144$ BS antennas. Although the Frobenius norm is a sensible measure of the overall correlation, it is not simple to interpret the numerical values. Hence, as discussed in Sec. VI we also indicate the correlation coefficients, α, of the classical exponential correlation model which correspond to the selected abscissa values. The figure clearly demonstrates the increase in correlation due to the sparsity of the channel. With Scenario 2, the equivalent median α is small, ranging from 0.495 to 0.936. In contrast, for the sparser channels in Scenario 1 we observe much larger median α values in the range of 0.886 to 0.994. Furthermore, we observe greater correlation in the VURA as compared to the HURA, and in the HURA as compared to the ULA. Given the angle spread is greater in the azimuth domain than the elevation domain, the antenna footprint in this direction is a dominant factor in the resulting correlation. As previously mentioned, the ULA has the greatest footprint in the azimuth domain, and hence the least correlation, followed by the HURA and finally the VURA.

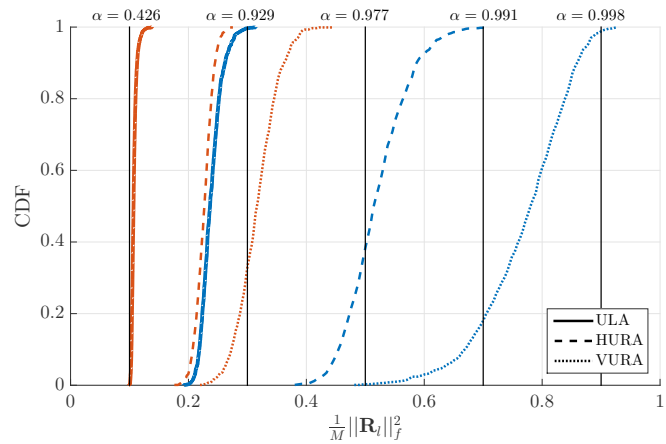

Fig. 8. CDF of the squared norm of the local correlation matrix, normalized by $M = 144$, for three array types and Scenarios 1 (in blue) and 2 (in red).

VIII. Conclusions

The vast body of papers in the massive MIMO literature consider statistical channel models for the performance characterization. Our paper moves the state-of-the-art by innovating analytical solutions for the more physically motivated ray-based channel models. We have derived accurate expressions for ZF SNR and MMSE SINR, and the resulting spectral efficiencies for ray-based channel models. The results, applicable to different antenna configurations and parameter distributions, offer important insights into the effects of the propagation environment. We have demonstrated an improvement in performance when moving from VURA to HURA to ULA antenna configurations, and a corresponding increase in the robustness to propagation scenarios. We have also investigated the impact of different array configurations and system parameters on the rate of convergence to favorable propagation. Finally, we evaluated the spatial correlation properties of ray-based models.

Appendix A
Proof of Proposition 1

From Property 1 and (1) we have

$$Y_l \triangleq \mathbb{E}[(\mathbf{H}^H\mathbf{H}\mathbf{X}^{-1}\mathbf{H}^H\mathbf{H})_{l,l}] =$$
$$\mathbb{E}\left[\sum_{l'=1}^{L}(\mathbf{h}_l^H\mathbf{h}_{l'})(\mathbf{X}^{-1})_{l',l'}(\mathbf{h}_{l'}^H\mathbf{h}_l)\right]$$
$$= \sum_{l'=1}^{L}\frac{1}{M\beta^{(l')}}\mathbb{E}\left[\sum_{c,s}^{C,S}\sum_{\hat{c},\hat{s}}^{C,S}\sum_{c',s'}^{C,S}\sum_{\hat{c}',\hat{s}'}^{C,S}\gamma_{c,s}^{(l)*}\gamma_{\hat{c},\hat{s}}^{(l')}\gamma_{c',s'}^{(l')*}\gamma_{\hat{c}',\hat{s}'}^{(l)}\right.$$
$$\left.\times\,\mathbf{a}^H(\theta_{c,s}^{(l)},\phi_{c,s}^{(l)})\mathbf{a}(\theta_{\hat{c},\hat{s}}^{(l')}\phi_{\hat{c},\hat{s}}^{(l')})\mathbf{a}^H(\theta_{c',s'}^{(l')}\phi_{c',s'}^{(l')})\mathbf{a}(\theta_{\hat{c}',\hat{s}'}^{(l)}\phi_{\hat{c}',\hat{s}'}^{(l)})\right], \tag{44}$$

where $\sum_{c,s}^{C,S}$ denotes the double sum $\sum_{c=1}^{C}\sum_{s=1}^{S}$ Next, using Property 2, the definition of κ and the fact that $\mathbf{a}^H(\theta_{c,s}^{(l)}\phi_{c,s}^{(l)})\mathbf{a}(\theta_{c,s}^{(l)}\phi_{c,s}^{(l)}) = M$, we have

$$\begin{aligned} Y_l = &\sum_{l'=1,l'\neq l}^{L} \frac{M}{\beta^{(l')}} \sum_{c,s}^{C,S}\sum_{\hat{c},\hat{s}}^{C,S} \beta_{c,s}^{(l)}\beta_{\hat{c},\hat{s}}^{(l')}\kappa + \\ &\frac{1}{M\beta^{(l)}}\left(\sum_{c,s}^{C,S}\sum_{c',s'\neq c,s}^{C,S}\beta_{c,s}^{(l)}\beta_{c',s'}^{(l)}M^2 + \sum_{c,s}^{C,S}\beta_{c,s}^{(l)2}M^2\right) + \\ &\frac{1}{M\beta^{(l)}}\sum_{c,s}^{C,S}\sum_{\hat{c},\hat{s}\neq c,s}^{C,S}\beta_{c,s}^{(l)}\beta_{\hat{c},\hat{s}}^{(l)}\mathbb{E}[|\mathbf{a}^H(\theta_{c,s}^{(l)}\phi_{c,s}^{(l)})\mathbf{a}(\theta_{\hat{c},\hat{s}}^{(l)}\phi_{\hat{c},\hat{s}}^{(l)})|^2], \\ &\triangleq T_1 + T_2 + T_3, \end{aligned} \tag{45}$$

where $\sum_{c',s'\neq c,s}^{C,S}$ denotes the sum $\sum_{c'=1}^{C}\sum_{s'=1}^{S}$ excluding the case subray $s' = s$ in cluster $c' = c$. The expectation in T_3 is $M^2\kappa$ whenever $c \neq \hat{c}$, as here the two rays are independent. When $c = \hat{c}$ the term is different. Out of the LC^2S^2 terms in the overall summation in (45), only $CS(S-1)$ contain this case. The exact calculation of these cases is possible, but results in a large increase in complexity with almost no improvement in accuracy for typical values of L, C, S, such as those considered in Table I. Hence, we approximate these cases by assuming that $\mathbb{E}[|\mathbf{a}^H(\theta_{c,s}^{(l)}\phi_{c,s}^{(l)})\mathbf{a}(\theta_{\hat{c},\hat{s}}^{(l)}\phi_{\hat{c},\hat{s}}^{(l)})|^2] \approx M^2\kappa$ for all $c, s, \hat{c}, \hat{s}$. This results in a slight underestimate of Y_l which gives a very tight lower bound. Substituting the approximation into T_3 and using $\sum_{\hat{c},\hat{s}}^{C,S}\beta_{\hat{c},\hat{s}}^{(l')} = \beta^{(l')}$ and $\sum_{c,s}^{C,S}\beta_{c,s}^{(l)} = \beta^{(l)}$ in T_1 gives Y_l as

$$Y_l \approx M\kappa\sum_{l'=1,l'\neq l}^{L}\beta^{(l)} + T_2 + M\kappa\sum_{c,s}^{C,S}\sum_{\hat{c},\hat{s}\neq c,s}^{C,S}\beta_{c,s}^{(l)}\beta_{\hat{c},\hat{s}}^{(l)}/\beta^{(l)}. \tag{46}$$

Next, merging the two sums in T_2 gives $T_2 = M\beta^{(l)}$. Finally, we note that

$$\beta^{(l)2} = \sum_{c,s}^{C,S}\sum_{\hat{c},\hat{s}\neq c,s}^{C,S}\beta_{c,s}^{(l)}\beta_{\hat{c},\hat{s}}^{(l)} + \sum_{c,s}^{C,S}\beta_{c,s}^{(l)2}. \tag{47}$$

Substituting (47) and $T_2 = M\beta^{(l)}$ into (46) gives

$$Y_l \approx M\kappa L\beta^{(l)} + M\beta^{(l)} - M\kappa\sum_{c,s}^{C,S}\beta_{c,s}^{(l)2}/\beta^{(l)}. \tag{48}$$

Substituting (48) into (19) and using $\mathbf{X}_{l,l} = M\beta^{(l)}$ gives (20) as desired.

Appendix B
Proof of Proposition 2

As shown in [31], $\mathbf{Q}_l = \lim_{M\to\infty}\mathbf{H}_l^H\mathbf{H}_l/M$ is given by $\mathbb{E}[\mathbf{H}_l^H\mathbf{H}_l/M]$. From Property 1 it follows that $\mathbf{Q}_l = \text{diag}(\beta^{(1)}, \dots \beta^{(l-1)}, \beta^{(l+1)} \dots \beta^{(L)})$. Since $\mathbf{Q}_l$ is diagonal, the matrix $(\mathbf{I} + \rho M\mathbf{Q}_l)^{-1}$ in the definition of $\mathbf{T}_l$ is also diagonal and is written as $\text{diag}(t_1, \dots t_{l-1}, t_{l+1}, \dots t_L)$, where $t_i = (1 + \rho M\beta^{(i)})^{-1}$. With this notation,

$$\begin{aligned} \mathbf{T}_l = \mathbb{E}[\mathbf{H}_l(\mathbf{I} + \rho M\mathbf{Q}_l)^{-1}\mathbf{H}_l^H] &= \sum_{i=1,i\neq l}^{L} t_i\mathbb{E}[\mathbf{h}_i\mathbf{h}_i^H] \\ &= \sum_{i=1,i\neq l}^{L} t_i\sum_{c,s}^{C,S}\sum_{\hat{c},\hat{s}}^{C,S}\mathbb{E}[\gamma_{c,s}^{(i)}\gamma_{\hat{c},\hat{s}}^{(i)*}\mathbf{a}(\theta_{c,s}^{(i)},\phi_{c,s}^{(i)})\mathbf{a}^H(\theta_{\hat{c},\hat{s}}^{(i)}\phi_{\hat{c},\hat{s}}^{(i)})] \\ &= \sum_{i=1,i\neq l}^{L} t_i\sum_{c,s}^{C,S}\beta_{c,s}^{(i)}\mathbb{E}[\mathbf{a}(\theta_{c,s}^{(i)},\phi_{c,s}^{(i)})\mathbf{a}^H(\theta_{c,s}^{(i)}\phi_{c,s}^{(i)})] \\ &= \sum_{i=1,i\neq l}^{L} t_i\beta^{(i)}\mathbf{A}, \end{aligned} \tag{49}$$

where $\mathbf{A}$ is the correlation matrix of an arbitrary steering vector given by $\mathbf{A} = \mathbb{E}[\mathbf{a}(\theta_{c,s}^{(i)},\phi_{c,s}^{(i)})\mathbf{a}^H(\theta_{c,s}^{(i)}\phi_{c,s}^{(i)})]$ and we have used Property 2 for the ray coefficients. Using Property 1 and (49) in (25) gives

$$\mathbb{E}[\text{SINR}_l^{\text{MMSE}}] \approx \rho M\beta^{(l)} - \rho^2\sum_{i=1,i\neq l}^{L} t_i\beta^{(i)}\mathbb{E}[\mathbf{h}_l^H\mathbf{A}\mathbf{h}_l]. \tag{50}$$

Expanding the expectation in (50) gives

$$\begin{aligned} \mathbb{E}[\mathbf{h}_l^H\mathbf{A}\mathbf{h}_l] &= \sum_{c,s}^{C,S}\sum_{\hat{c},\hat{s}}^{C,S}\mathbb{E}[\gamma_{c,s}^{(l)*}\gamma_{\hat{c},\hat{s}}^{(l)}\mathbf{a}^H(\theta_{c,s}^{(l)},\phi_{c,s}^{(l)})\mathbf{A}\mathbf{a}(\theta_{\hat{c},\hat{s}}^{(l)},\phi_{\hat{c},\hat{s}}^{(l)})] \\ &= \sum_{c,s}^{C,S}\beta_{c,s}^{(l)}\mathbb{E}[\mathbf{a}^H(\theta_{c,s}^{(l)},\phi_{c,s}^{(l)})\mathbf{A}\mathbf{a}(\theta_{c,s}^{(l)},\phi_{c,s}^{(l)})] \\ &= \beta^{(l)}\sum_{i=1}^{M}\sum_{j=1}^{M}(\mathbf{A})_{i,j}(\mathbf{A})_{j,i} = \beta^{(l)}||\mathbf{A}||_F^2, \end{aligned} \tag{51}$$

from the definition of $\mathbf{A}$ and Property 2. Note that defining the vectors $\mathbf{x} = \mathbf{a}(\theta_{c,s}^{(l)},\phi_{c,s}^{(l)}) = (x_1, x_2, \dots, x_M)^T$ and $\mathbf{y} = \mathbf{a}(\theta_{\hat{c},\hat{s}}^{(l)},\phi_{\hat{c},\hat{s}}^{(l)}) = (y_1, y_2, \dots, y_M)^T$, as steering vectors for two independent rays gives $M^2\kappa = \mathbb{E}[|\mathbf{x}^H\mathbf{y}|^2]$. Using this notation, we have

$$M^2\kappa = \sum_{i=1}^{M}\sum_{\hat{i}=1}^{M}\mathbb{E}[x_i^*x_{\hat{i}}]\mathbb{E}[y_iy_{\hat{i}}^*] = \sum_{i=1}^{M}\sum_{\hat{i}=1}^{M}|\mathbb{E}[x_i^*x_{\hat{i}}]|^2 = ||\mathbf{A}||_F^2. \tag{52}$$

Substituting $||\mathbf{A}||_F^2 = M^2\kappa$ into (51) and (51) into (50) gives the desired result in (26).

Appendix C
Proof of Lemma 1

Let $f(\phi)$ denote the PDF of ϕ and $f_w(\phi)$ its wrapped equivalent on $[-\pi, \pi]$. The required expectation is

$$\mathbb{E}[e^{jz\sin\phi}] = \int_{-\infty}^{\infty} e^{jz\sin\phi}f(\phi)d\phi = \int_{-\pi}^{\pi} e^{jz\sin\phi}f_w(\phi)d\phi. \tag{53}$$

Now, for any wrapped PDF over $[-\pi, \pi]$ [46], we have

$$f_w(\phi) = \frac{1}{2\pi}\sum_{n=-\infty}^{\infty}\psi(n)e^{-jn\phi}, \tag{54}$$

where

$$\psi(n) = \mathbb{E}[e^{jn\phi}] = \int_{-\infty}^{\infty} e^{jn\phi}f(\phi)d\phi. \tag{55}$$

Hence,

$$\mathbb{E}[e^{jz\sin\phi}] = \int_{-\pi}^{\pi} e^{jz\sin\phi}\frac{1}{2\pi}\sum_{n=-\infty}^{\infty}\psi(n)e^{-jn\phi}d\phi$$
$$= \frac{1}{2\pi}\sum_{n=-\infty}^{\infty}\psi(n)\int_{-\pi}^{\pi}e^{j(z\sin\phi - n\phi)}d\phi. \quad (56)$$

The integral in (56) can be computed as

$$\int_{-\pi}^{\pi} e^{j(z\sin\phi - n\phi)}d\phi = 2\int_0^{\pi}\cos(z\sin x - nx)dx = 2\pi J_n(z), \quad (57)$$

using [47, pp. 452-453]. Hence, the answer follows.

Appendix D
Proof of Lemma 2

Starting with (36), we have

$$H_h(z_1,z_2) = \mathbb{E}\left[e^{jz_1\sin\theta\sin\phi + jz_2\sin\theta\cos\phi}\right]$$
$$= \mathbb{E}\left[e^{jz_T\sin\theta\sin(\phi+A)}\right], \quad (58)$$

where $z_T = \sqrt{z_1^2+z_2^2}$ and $A = \tan^{-1}(z_2/z_1)$. Applying Lemma 1 gives

$$\mathbb{E}\left[e^{jz_T\sin\theta\sin(\phi+A)}\right] = \sum_{n=-\infty}^{\infty}\hat{\psi}(n)J_n(z_T\sin\theta), \quad (59)$$

where $\hat{\psi}(n) = \mathbb{E}[e^{jn(\phi+A)}] = e^{jnA}\psi(n)$. Hence,

$$H_h(z_1,z_2) = \sum_{n=-\infty}^{\infty}\psi(n)e^{jnA}\mathbb{E}[J_n(z_T\sin\theta)]. \quad (60)$$

Using the same approach as in (54), but altering the wrapping from $[-\pi,\pi]$ to $[0,\pi]$, we can write the wrapped elevation PDF, $f_w(\theta)$, on $[0,\pi]$ as

$$f_w(\theta) = \frac{1}{\pi}\sum_{m=-\infty}^{\infty}(-1)^m e^{-2mj\theta}\chi(2m), \quad (61)$$

where $\chi(\cdot)$ is the CF of the unwrapped PDF, $f_\theta(\theta)$. Hence,

$$H_h(z_1,z_2) = \frac{1}{\pi}\sum_{n=-\infty}^{\infty}\sum_{m=-\infty}^{\infty}\psi(n)\chi(2m)e^{jnA}(-1)^m\times$$
$$\int_0^{\pi}e^{-2mj\theta}J_n(z_T\sin\theta)d\theta. \quad (62)$$

Breaking up the integral in (62) into real and imaginary terms and using [48, Equations 6.681.8 and 6.681.9] gives the desired result in (37).

Appendix E
Proof of Lemma 3

By definition,

$$H_v(z_1,z_2) = \mathbb{E}_\theta\left[e^{jz_1\cos\theta}\mathbb{E}_\phi[e^{jz_2\sin\theta\cos\phi}]\right]. \quad (63)$$

Writing $\cos\phi = \sin(\phi+\pi/2)$ and using (59) gives

$$H_v(z_1,z_2) = \mathbb{E}_\theta\left[e^{jz_1\cos\theta}\sum_{n=-\infty}^{\infty}\psi(n)e^{jn\pi/2}J_n(z_2\sin\theta)\right]. \quad (64)$$

Hence, the result in (40) follows.

Appendix F
Rate of convergence

To analyse the rate of convergence of analytical results to the true expectation κ, we define ϵ_{ULA}, ϵ_{HURA} and ϵ_{VURA} as the error resulting from the truncation of the infinite sums in (33), (37) and (40), respectively. In order to bound these error terms we require the following well-known results

$$|J_n(z)| \le 1/\sqrt{2} \quad \forall z \quad \text{if} \quad |n| \ge 1, \quad (65)$$
$$J_{-n}(z) = (-1)^n J_n(z), \quad (66)$$
$$\sum_{n=K}^{\infty} g(n) \le \int_{K-1}^{\infty} g(x)dx, \quad (67)$$

for any decreasing function, $g(x)$, such that the integral in (67) exists. Using (65)-(67), the error term, ϵ_{ULA}, in the approximation of (35) for a ULA can be bounded as

$$|\epsilon_{\text{ULA}}| \le 2\sum_{n=N+1}^{\infty}\frac{e^{-n^2\sigma_{\text{c}}^2/2}}{1+n^2\sigma_{\text{s}}^2}|J_n(z)| \le \frac{\sqrt{2}}{\sigma_{\text{s}}^2}\sum_{n=N+1}^{\infty}\frac{e^{-n^2\sigma_{\text{c}}^2/2}}{n^2}$$
$$\le \frac{\sqrt{2}}{\sigma_{\text{s}}^2}\int_N^{\infty}\frac{e^{-x^2\sigma_{\text{c}}^2/2}}{x^2}dx \le \frac{\sqrt{2}}{N\sigma_{\text{s}}^2}e^{-N^2\sigma_{\text{c}}^4/4} \quad (68)$$

where the final inequality in (68) comes from [48, Equation 3.461.1] by neglecting a negative term in the formula for the integral. Hence, $\epsilon_{\text{ULA}} \to 0$ extremely rapidly as $N \to \infty$ and any desired error bound, ϵ_{target}, can be achieved by finding the minimum value of N which solves

$$\epsilon_{\text{target}} = \frac{\sqrt{2}}{N\sigma_{\text{s}}^2}e^{-N^2\sigma_{\text{c}}^4/4}. \quad (69)$$

For a vertical URA, the error bound is the same. Let ϵ_{VURA} be the error term in using a truncation of (40) to the range $-N \le n \le N$. Since $|\mathbb{E}[e^{jz_1\cos\theta}J_n(z_2\sin\theta)]| \le \mathbb{E}[|e^{jz_1\cos\theta}||J_n(z_2\sin\theta)|] \le 1/\sqrt{2}$ from (65), we can write $|\epsilon_{\text{VURA}}| \le \sqrt{2}\sum_{n=N+1}^{\infty}|\psi(n)|$ giving the same bound as in (68) so that the desired accuracy can be achieved by solving (69).

For a horizontal URA, truncating (37) gives the expression

$$H_h(z_1,z_2) = \sum_{m=-T}^{T}\sum_{n=-N}^{N}c(m,n) + \epsilon_{\text{HURA}}, \quad (70)$$

where $c(m,n) = (-1)^{p(n)}\psi(n)\chi(2m)e^{jnA}I(m,n)$. Hence, the error is bounded by

$$|\epsilon_{\text{HURA}}| \le \sum_{m=-\infty}^{\infty}\left(\sum_{n=N+1}^{\infty}|c(m,n)| + \sum_{n=-\infty}^{-(N+1)}|c(m,n)|\right)$$
$$+ \sum_{n=-\infty}^{\infty}\left(\sum_{m=T+1}^{\infty}|c(m,n)| + \sum_{m=-\infty}^{-(T+1)}|c(m,n)|\right). \quad (71)$$

If $N \le 2T$, then the indices in (71) satisfy $||n|/2 \pm m| \ge 1$ and we can use (65) to give $|I(m,n)| \le 1/2$. Hence, $|c(m,n)| \le \frac{1}{2}|\psi(n)||\chi(2m)|$ and using the CF bounds in (68) we have

$$|c(m,n)| \le \frac{e^{-n^2\sigma_{\text{c}}^2/2}}{n^2}\frac{1}{m^4}\frac{1}{32\sigma_{\text{c}}^2\hat{\sigma}_{\text{c}}^2\hat{\sigma}_{\text{s}}^2} \triangleq a(n)b(m)\zeta, \quad (72)$$

for $n \neq 0$ and $|c(m,0)| \leq \frac{1}{2}|\chi(2m)| \leq b(m)\sigma_{\rm c}^2\zeta$. This gives the bound

$$|\epsilon_{\rm HURA}| \leq 2\zeta \sum_{n=N+1}^{\infty} a(n) \sum_{m=-\infty}^{\infty} b(m) + 2\zeta \sum_{m=T+1}^{\infty} b(m) \sum_{\substack{n=-\infty \\ n \neq 0}}^{\infty} a(n) + 2\sigma_{\rm c}^2\zeta \sum_{m=T+1}^{\infty} b(m). \tag{73}$$

We state the following results which arise from (67), (68) and well known results on sums of reciprocal powers

$$\begin{aligned} \sum_{m=-\infty}^{\infty} b(m) &= \sum_{m=-\infty}^{\infty} \frac{1}{m^4} = 1 + \frac{2\pi^4}{90}, \\ \sum_{m=T+1}^{\infty} b(m) &\leq \int_T^{\infty} \frac{1}{x^4} dx = \frac{1}{3T^3}, \\ \sum_{n=N+1}^{\infty} a(n) &\leq \frac{e^{-N^2\sigma_{\rm c}^4/4}}{N}, \\ \sum_{n=-\infty, n\neq 0}^{\infty} a(n) &= 2\sum_{n=1}^{\infty} a(n) < 2\sum_{n=1}^{\infty} \frac{1}{n^2} = \frac{\pi^3}{3}. \end{aligned} \tag{74}$$

Substituting these bounds in (74) gives

$$|\epsilon_{\rm HURA}| \leq \frac{2\zeta}{N}\left(1 + \frac{2\pi^4}{90}\right) e^{-N^2\sigma_{\rm c}^4/4} + \frac{2\zeta}{3T^3}\left(\sigma_{\rm c}^2 + \frac{\pi^2}{3}\right). \tag{75}$$

Clearly, $\epsilon_{\rm HURA} \to 0$ as $N \to \infty$ and $T \to \infty$ so the sum is convergent. Equating the right hand side of (75) to $\epsilon_{\rm target}$ and solving for N and T guarantees the desired accuracy.

References

[1] C. L. Miller, P. A. Dmochowski, P. J. Smith, H. Tataria, and M. Matthaiou, "Multi-user processing for ray-based channels," in *Proc. IEEE ICC*, May 2019.

[2] T. L. Marzetta, "Noncooperative cellular wireless with unlimited numbers of base station antennas," *IEEE Trans. Wireless Commun.*, vol. 9, no. 11, pp. 3590–3600, Nov. 2010.

[3] H. Q. Ngo, E. G. Larsson, and T. L. Marzetta, "Energy and spectral efficiency of very large multiuser MIMO systems," *IEEE Trans. Commun.*, vol. 61, no. 4, pp. 1436–1449, Apr. 2013.

[4] E. Björnson, E. G. Larsson, and M. Debbah, "Massive MIMO for maximal spectral efficiency: How many users and pilots should be allocated?" *IEEE Trans. Wireless Commun.*, vol. 15, no. 2, pp. 1293–1308, Feb. 2016.

[5] Y.-G. Lim, C.-B. Chae, and G. Caire, "Performance analysis of massive MIMO for cell-boundary users," *IEEE Trans. Wireless Commun.*, vol. 14, no. 12, pp. 6827–6842, Dec. 2015.

[6] A. Khansefid and H. Minn, "Achievable downlink rates of MRC and ZF precoders in massive MIMO with uplink and downlink pilot contamination," *IEEE Trans. Commun.*, vol. 63, no. 12, pp. 4849–4864, Dec. 2015.

[7] H. Yang and T. L. Marzetta, "Massive MIMO with max-min power control in line-of-sight propagation environment," *IEEE Trans. Commun.*, vol. 65, no. 11, pp. 4685–4693, Nov. 2017.

[8] H. Tataria, P. J. Smith, L. J. Greenstein, P. A. Dmochowski, and M. Matthaiou, "Impact of line-of-sight and unequal spatial correlation on uplink MU-MIMO systems," *IEEE Wireless Commun. Lett.*, vol. 6, no. 5, pp. 634–637, Oct. 2017.

[9] H. Tataria, P. J. Smith, and P. A. Dmochowski, "On the general analysis of coordinated regularized zero-forcing precoding: An application to two-tier small-cell networks," *IEEE Trans. Commun.*, vol. 65, no. 7, pp. 3133–3150, Apr. 2017.

[10] H. Tataria, P. J. Smith, M. Matthaiou, H. Q. Ngo, and P. A. Dmochowski, "Revisiting MMSE combining for massive MIMO over heterogeneous propagation channels," in *Proc. IEEE ICC*, Jun. 2018.

[11] Ö. Özdogan, E. Björnson, and E. G. Larsson, "Uplink spectral efficiency of massive MIMO with spatially correlated Rician fading," in *Proc. IEEE SPAWC*, Jun. 2018, pp. 1–5.

[12] S. Sangodoyin, V. Kristem, C. U. Bas, M. Käske, J. Lee, C. Schneider, G. Sommerkorn, C. J. Zhang, R. Thomä, and A. F. Molisch, "Cluster characterization of 3-D MIMO propagation channel in an urban macrocellular environment," *IEEE Trans. Wireless Commun.*, vol. 17, no. 8, pp. 5076–5091, Aug. 2018.

[13] J. Ko, Y.-J. Cho, S. Hur, T. Kim, J. Park, A. F. Molisch, K. Haneda, M. Peter, D.-J. Park, and D.-H. Cho, "Millimeter-wave channel measurements and analysis for statistical spatial channel model in in-building and urban environments at 28 GHz," *IEEE Trans. Wireless Commun.*, vol. 16, no. 9, pp. 5853–5868, Sep. 2017.

[14] X. Gao, O. Edfors, F. Rusek, and F. Tufvesson, "Massive MIMO performance evaluation based on measured propagation data," *IEEE Trans. Wireless Commun.*, vol. 14, no. 7, pp. 3899–3911, Jul. 2015.

[15] M. R. Akdeniz, Y. Liu, M. K. Samimi, S. Sun, S. Rangan, T. S. Rappaport, and E. Erkip, "Millimeter wave channel modeling and cellular capacity evaluation," *IEEE J. Sel. Areas Commun.*, vol. 32, no. 6, pp. 1164–1179, Jun. 2014.

[16] 3GPP, "Study on channel model for frequencies from 0.5 to 100 GHz," 3rd Generation Partnership Project (3GPP), Tech. Rep. TR 38.901 (V14.2.0), Sep. 2017. [Online]. Available: http://www.3gpp.org/

[17] C. T. Neil, M. Shafi, P. J. Smith, P. A. Dmochowski, and J. Zhang, "Impact of microwave and mmWave channel models on 5G systems performance," *IEEE Trans. Antennas Propag.*, vol. 65, no. 12, pp. 6505–6520, Dec. 2017.

[18] X. Cheng and Y. He, "Channel modeling and analysis of ULA massive MIMO systems," in *Proc. IEEE ICACT*, Feb. 2018, pp. 411–416.

[19] V. Kristem, S. Sangodoyin, C. U. Bas, M. Käske, J. Lee, C. Schneider, G. Sommerkorn, C. J. Zhang, R. S. Thomae, and A. F. Molisch, "3D MIMO outdoor-to-indoor propagation channel measurement," *IEEE Trans. Wireless Commun.*, vol. 16, no. 7, pp. 4600–4613, Jul. 2017.

[20] H. Tataria and F. Tufvesson, "Impact of spatial consistency on dynamic beamforming for millimeter-wave cellular systems," in *Proc. COST IRACON*, Jan. 2019. [Online]. Available: http://www.iracon.org/meeting/9th-mc-meeting-and-9th-technical-meeting/

[21] X. Wu, N. C. Beaulieu, and D. Liu, "On favorable propagation in massive MIMO systems and different antenna configurations," *IEEE Access*, vol. 5, pp. 5578–5593, Apr. 2017.

[22] Z. Gao, L. Dai, C. Yuen, and Z. Wang, "Asymptotic orthogonality analysis of time-domain sparse massive MIMO channels," *IEEE Commun. Lett.*, vol. 19, no. 10, pp. 1826–1829, Oct. 2015.

[23] J. Chen, "When does asymptotic orthogonality exist for very large arrays?" in *Proc. IEEE GLOBECOM*, Dec. 2013, pp. 4146–4150.

[24] C. Masouros and M. Matthaiou, "Space-constrained massive MIMO: Hitting the wall of favorable propagation," *IEEE Commun. Lett.*, vol. 19, no. 5, pp. 771–774, May 2015.

[25] H. Q. Ngo, E. G. Larsson, and T. L. Marzetta, "Aspects of favorable propagation in massive MIMO," in *Proc. EUSIPCO*, Sep. 2014, pp. 76–80.

[26] N. Rupasinghe, Y. Yapici, J. I. Vergara, and I. Guvenc, "Impact of angular spread in moderately large MIMO systems under pilot contamination," *IEEE Trans. Veh. Technol.*, vol. 67, no. 11, Nov. 2018.

[27] R. Shafin and L. Liu, "Multi-cell multi-user massive FD-MIMO: Downlink precoding and throughput analysis," *IEEE Trans. Wireless Commun.*, vol. 18, no. 1, pp. 487–502, Jan. 2019.

[28] H. Tataria, M. Matthaiou, P. J. Smith, V. F. Fusco, and G. C. Alexandropoulos, "Impact of RF processing and switching errors in lens-based massive MIMO systems," in *Proc. 2018 IEEE SPAWC*, Jun. 2018, pp. 1–5.

[29] Y. Han, S. Jin, J. Zhang, J. Zhang, and K.-K. Wong, "DFT-based hybrid beamforming multiuser systems: Rate analysis and beam selection," *IEEE J. Sel. Topics in Signal Process.*, vol. 12, no. 3, pp. 514–528, Jun. 2018.

[30] L. Zhao, D. W. K. Ng, and J. Yuan, "Multi-user precoding and channel estimation for hybrid millimeter wave systems," *IEEE J. Sel. Areas Commun.*, vol. 35, no. 7, pp. 1576–1590, Jul. 2017.

[31] S. Li, P. J. Smith, P. A. Dmochowski, H. Tataria, M. Matthaiou, and J. Yin, "Massive MIMO for ray-based channels," in *Proc. IEEE ICC*, May 2019.

[32] E. G. Larsson, T. L. Marzetta, H. Q. Ngo, and H. Yang, "Antenna count for massive MIMO: 1.9 GHz versus 60

GHz," *CoRR*, vol. abs/1702.06111, Jul. 2017. [Online]. Available: http://arxiv.org/abs/1702.06111

[33] H. Tataria, P. J. Smith, A. Molisch, S. Sangodoyin, M. Matthaiou, P. A. Dmochowski, J. Zhang, and R. S. Thoma, "Spatial correlation variability in multiuser systems," in *Proc. IEEE ICC*, May 2018, pp. 1–7.

[34] H. Tataria, P. J. Smith, L. J. Greenstein, P. A. Dmochowski, and M. Shafi, "Performance and analysis of downlink multiuser MIMO systems with regularized zero-forcing precoding in Ricean fading channels," in *Proc. IEEE ICC*, May 2016, pp. 1–7.

[35] S. Biswas, C. Masouros, and T. Ratnarajah, "On the energy efficiency of massive MIMO with space-constrained 2D antenna arrays," in *Proc. IEEE ICC*, May 2016, pp. 1–6.

[36] Q. Nadeem, A. Kammoun, and M. Alouini, "Elevation beamforming with full dimension MIMO architectures in 5G systems: A tutorial," *CoRR*, vol. abs/1805.00225, Aug. 2018. [Online]. Available: http://arxiv.org/abs/1805.00225

[37] H. Tataria, "Analysis of multiuser cellular systems over heterogeneous channels," Ph.D. dissertation, Victoria University of Wellington, 2017.

[38] D. Zhu, B. Li, and P. Liang, "On the matrix inversion approximation based on Neumann series in massive MIMO systems," in *Proc. IEEE ICC*, Jun. 2015, pp. 1763–1769.

[39] M. Roy, S. Paquelet, L. L. Magoarou, and M. Crussière, "MIMO channel hardening: A physical model based analysis," *CoRR*, vol. abs/1804.07491, 2018.

[40] S. Gunnarsson, J. Flordelis, L. V. der Perre, and F. Tufvesson, "Channel hardening in massive MIMO - a measurement based analysis," *in Proc. 2018 IEEE SPAWC*, pp. 1–5, Jun. 2018.

[41] M. Matthaiou, P. J. Smith, H. Q. Ngo, and H. Tataria, "Does massive MIMO fail in Ricean channels?" *IEEE Wireless Commun. Letters*, vol. 8, no. 1, pp. 61–64, Feb. 2019.

[42] P. J. Smith, R. Senanayake, and P. A. Dmochowski, "How accurate is your Gaussian/gamma approximation?" *IEEE Trans. Wireless Commun.*, vol. 7, no. 5, pp. 804–807, Oct. 2018.

[43] Z. Zhong, X. Yin, X. Li, and X. Li, "Extension of ITU IMT-advanced channel models for elevation domains and line-of-sight scenarios," in *Proc. IEEE VTC*, Sep. 2013, pp. 1–5.

[44] H. Q. Ngo, *Massive MIMO: Fundamentals and system designs*. Linköping University Electronic Press, 2015, vol. 1642.

[45] B. Clerckx and C. Oestges, *MIMO Wireless Networks: Channels, Techniques and Standards for Multi-Antenna, Multi-User and Multi-Cell Systems*. Elsevier Science, 2013. [Online]. Available: https://books.google.co.nz/books?id=drEX1J7jHUIC

[46] K. V. Mardia, *Statistics of Directional Data*. Academic Press, 1972.

[47] N. M. Temme and D. Zwillinger, *Special Functions: An Introduction to the Classical Functions of Mathematical Physics*, 2nd ed. Wiley, 1996.

[48] I. S. Gradshteyn and I. M. Ryzhik, *Table of Integrals, Series, and Products*, 5th ed. Elsevier/Academic Press, Amsterdam, 1994.